

9

BUILDING BLOCKS FOR MULTIDIMENSIONAL NMR AND SPECIAL CONSIDERATIONS FOR BIOLOGICAL APPLICATIONS OF NMR

The development of multidimensional NMR (three or more frequency dimensions in a single experiment) is a logical extension from two-dimensional NMR. A third independent time variable introduced into a multipulse experiment results in a third independent frequency domain that can represent some other desired correlation between a set of spins. Although three-dimensional NMR experiments can be homonuclear (e.g. ^1H in all three dimensions), most often they are used to identify heteronuclear connectivity unambiguously, particularly in large macromolecules such as proteins or nucleic acids, and it is on these experiments that we will concentrate. Three-dimensional NMR experiments are most often applied to large molecules that are at low concentration relative to solvent (usually water); solvent signal and artifact suppression are therefore particularly important. Furthermore, selective excitation schemes are necessary in some experiments. These special topics will also be considered in the present chapter.

A three-dimensional NMR experiment can be thought of as a two-dimensional experiment in which the detection period (t_2) is replaced by a second two-dimensional experiment. This gives rise to a hybrid experiment in which the correlations expected in both two-dimensional experiments are observed, with three independent time variables (t_1 , t_2 and t_3) leading to three frequency dimensions after FT. Two of the first and still among the most commonly used three-dimensional NMR experiments, NOESY-HSQC and TOCSY-HSQC, combine the results of the homonuclear NOESY and TOCSY experiments with an HSQC

experiment that correlates directly bonded heteronuclei (Reference 1). The NOESY and TOCSY portions of the experiments connect ^1H spins either by through-space or through-bond interactions, respectively, the results of which are then edited according to the heteronucleus to which the receiver proton (the proton that is normally detected during t_2 in the two-dimensional experiment) is attached. We will first examine the NOESY- ^1H , ^{15}N HSQC as applied to a protein. If more than one NH proton in the molecule has the same chemical shift, there will be some ambiguity about which NOE cross-peak is assigned to which NH proton in the two-dimensional spectrum. However, even if two different NH groups are degenerate in ^1H chemical shift (a likely occurrence in large proteins), the homonuclear NOESY will give ambiguous results: it will not be possible to assign cross-peaks to a particular NH proton. However, simultaneous degeneracy of ^1H and ^{15}N chemical shifts is much less likely than degeneracy in only one dimension. Assuming

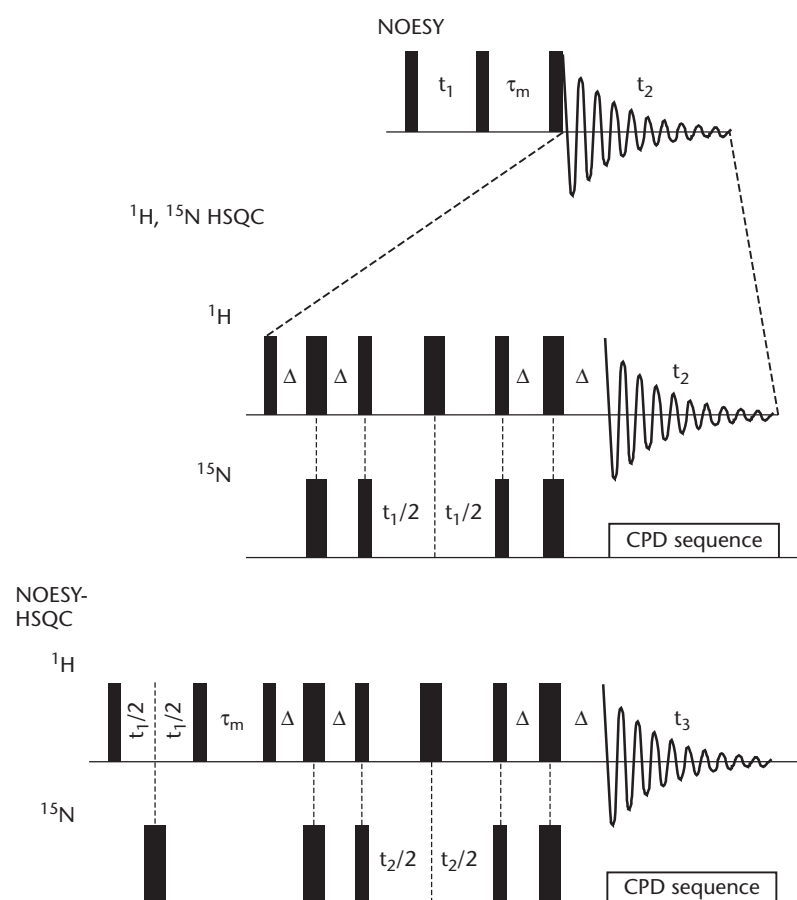


Figure 9.1 Combination of two two-dimensional sequences (NOESY and ^1H , ^{15}N HSQC) to yield a single three-dimensional sequence. Figure 9.2 shows the results of the three-dimensional experiment. Note that a ^{15}N π pulse has been added during the t_1 evolution period of the three-dimensional experiment in order to remove ^{15}N coupling to ^1H . The ^{15}N evolution time is called t_2 , and the detection period is called t_3 .

that the protein has been prepared in a ^{15}N -enriched form, one can imagine adding a ^1H , ^{15}N HSQC step that will label the observed ^1H coherences not only in terms of the NOEs involving that coherence, but also in terms of the ^{15}N chemical shift of the attached nitrogens. The net result is an experiment that sorts NOEs to NH protons according to the chemical shifts of their attached ^{15}N spins.

Figure 9.1 gives a conceptual picture of how the three-dimensional NOESY- ^1H , ^{15}N HSQC experiment is put together from two separate two-dimensional experiments. Figure 9.2 shows how the three-dimensional experiment resolves overlapping correlations in three dimensions. The resulting three-dimensional spectrum can be viewed in three different ways: (1) as a stack of two-dimensional ^1H , ^{15}N HSQC spectra that are edited according to the chemical shifts of protons from which the NH proton detects NOEs; (2) as a stack of NOESY spectra that are edited according to the chemical shift of the ^{15}N shifts of the nitrogens to which the detected amide protons are attached; or (3) as a stack of ^{15}N , ^1H correlation spectra

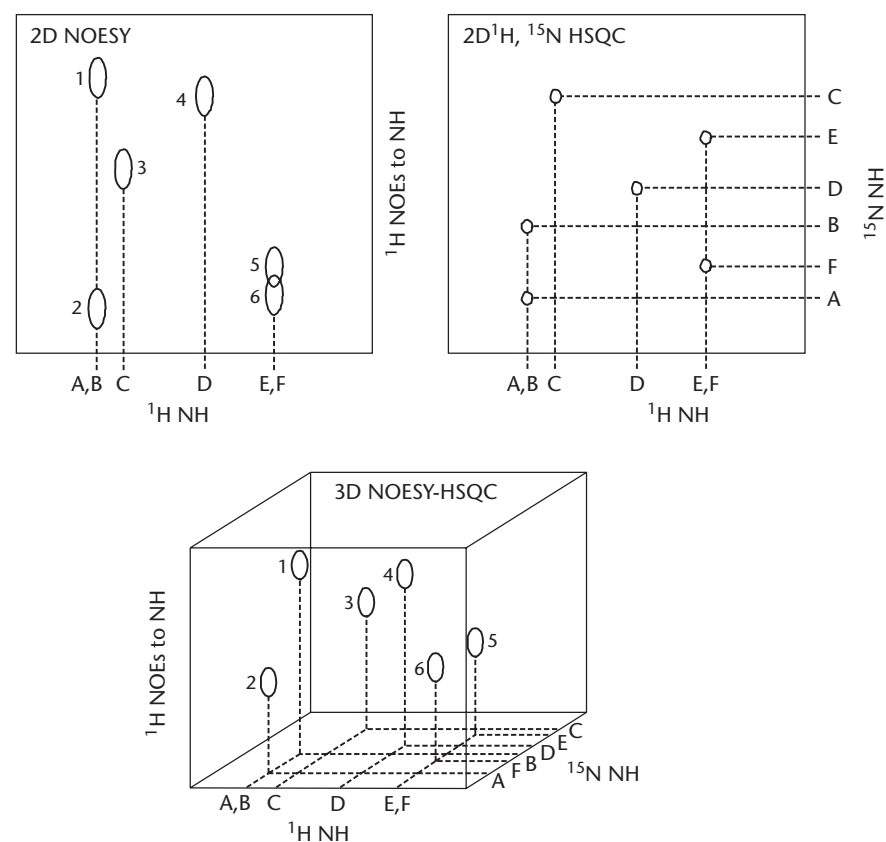


Figure 9.2 Diagram of spectral deconvolution by three-dimensional NMR. (Top left) NOESY spectrum showing ambiguous NOE connectivities; NOEs to NH protons A and B are overlapped, as are those to protons E and F. All NH correlations are unambiguously resolved in the ^1H , ^{15}N HSQC (upper right). The NOESY-HSQC (bottom) shows that all NOEs are unambiguously resolved in the third dimension.

244 Multidimensional NMR and biological applications

that show the chemical shifts of nitrogens versus the chemical shifts of protons that give NOEs to the NH attached to those nitrogens, and are edited by the chemical shift of the NH proton. Typically, the three-dimensional spectrum is analyzed in this fashion, rather than as a cube, which looks nice but is difficult to make sense of. Figures 9.3–9.7 show how such editing takes place and how it simplifies the analysis of signals that would otherwise be overlapped in two-dimensional experiments. Four-dimensional NMR, which we will not discuss in detail, takes this process one step further. In the four-dimensional case, we can imagine that the cube of the three-dimensional experiment has a vernier dial attached to it, marked with the chemical shift of the fourth correlation. As the dial is turned, cross-peaks within the three-dimensional cube appear and vanish according to whether or not they correlate with the chemical shift of the fourth dimension.

Although many three-dimensional experiments look (and are) quite complicated, they are generally put together from building blocks with which we are already familiar. Furthermore, the coherence transfer from protons to heteronuclei and

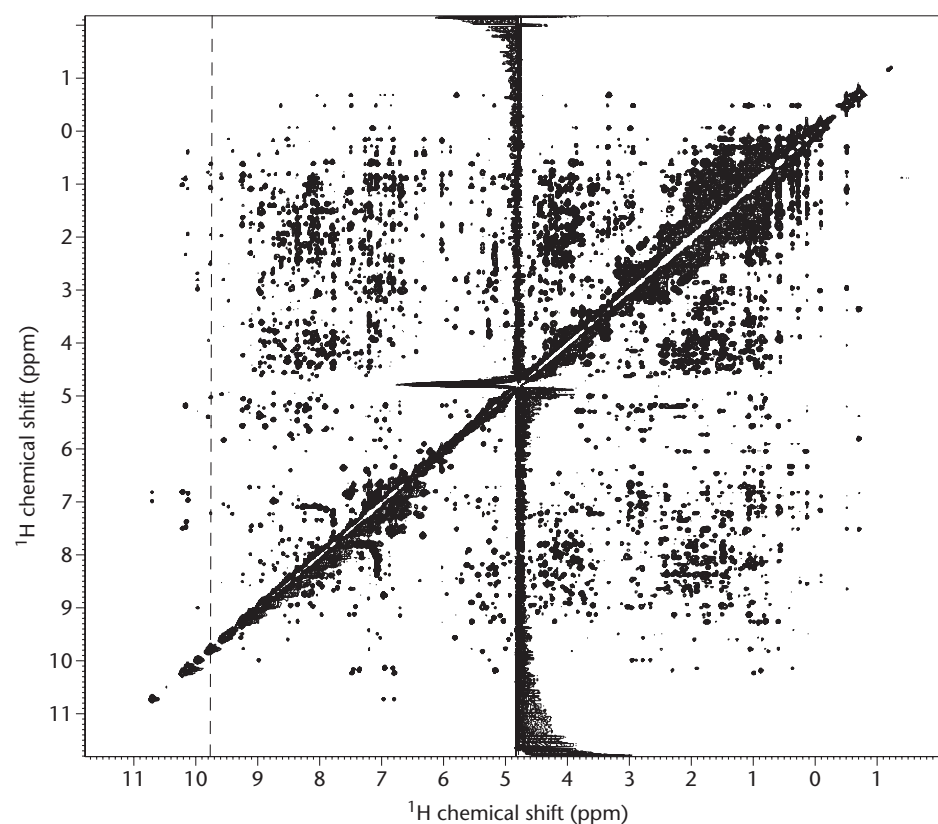


Figure 9.3 NOESY spectrum of 1 mM ^{15}N -labeled acireductone dioxygenase (ARD), a 179-residue metalloenzyme, in 90/10 $\text{H}_2\text{O}/\text{D}_2\text{O}$ acquired at 750 MHz with ^{15}N decoupling applied during acquisition. Dashed line indicates an amide chemical shift where two amino acid residues (Q123 and A152) are overlapped (see Figure 9.4).

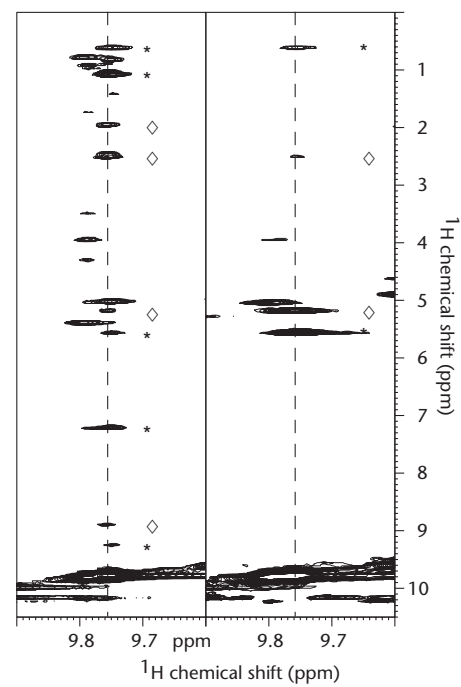


Figure 9.4 Two strips from the two-dimensional NOESY (left) and two-dimensional TOCSY (right) spectra of ^{15}N -labeled ARD in 90/10 $\text{H}_2\text{O}/\text{D}_2\text{O}$. The strips were extracted at the chemical shift indicated in Figure 9.3. *: Resonance correlated to A152; \diamond : resonance correlated to Q123.

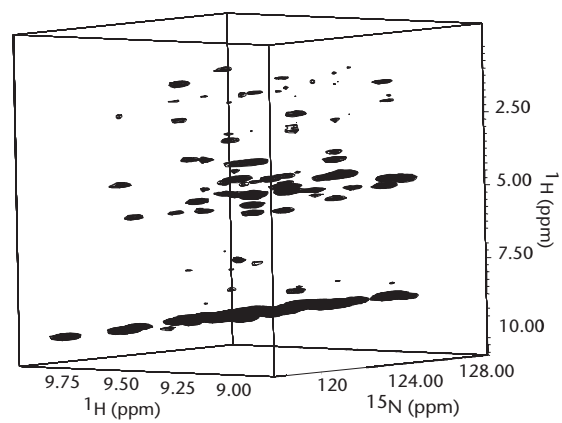


Figure 9.5 Three-dimensional (cubic) representation of the three-dimensional ^{15}N -edited NOESY spectrum of 1 mM ^{15}N -labeled ARD in 90/10 $\text{H}_2\text{O}/\text{D}_2\text{O}$ acquired at 750 MHz shown in Figures 9.3 and 9.4.

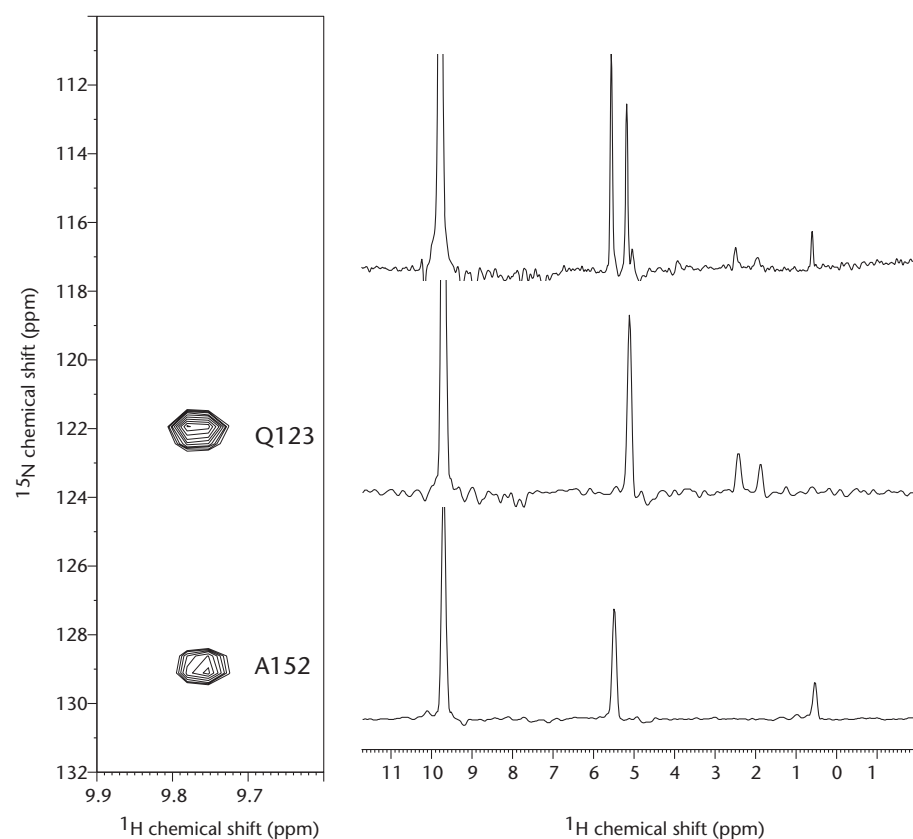


Figure 9.6 Three-dimensional ^{15}N -edited TOCSY spectrum of 1 mM ^{15}N -labeled ARD in 90/10 $\text{H}_2\text{O}/\text{D}_2\text{O}$ acquired at 750 MHz. The two-dimensional strip (left) is extracted at 9.75 ppm in the F2 (indirect ^1H) and F3 (observe ^1H) dimensions. The two amide ^{15}N chemical shifts can clearly be seen. On the right are one-dimensional slices through the three-dimensional spectrum at 129 ppm in ^{15}N (bottom), and at 122 ppm in ^{15}N (middle). The top slice is taken from the two-dimensional TOCSY shown in Figure 9.4.

back tends to simplify the phase cycling required in order to select exclusively for particular coherence transfer pathways. In these cases, if the transfer is unsuccessful, no signal will result, so the pulse sequences themselves act as efficient filters for spurious signals. Most three-dimensional heteronuclear experiments are designed to require a maximum of four steps in a phase cycle, no more than is required for difference spectroscopy in HMQC or HSQC (i.e. subtraction of signals is required for the appropriate isotope editing). If gradient coherence selection is used, even that minimum phase cycle is not required, although quadrature detection in indirectly detected dimensions still requires some phase cycling. However, as concentrations of the proteins and polynucleic acids that are typically the subject of three-dimensional experiments are often quite low, multiple scans at each (t_1, t_2) combination are often necessary anyway in order to obtain sufficient signal-to-noise ratio in the experiment.

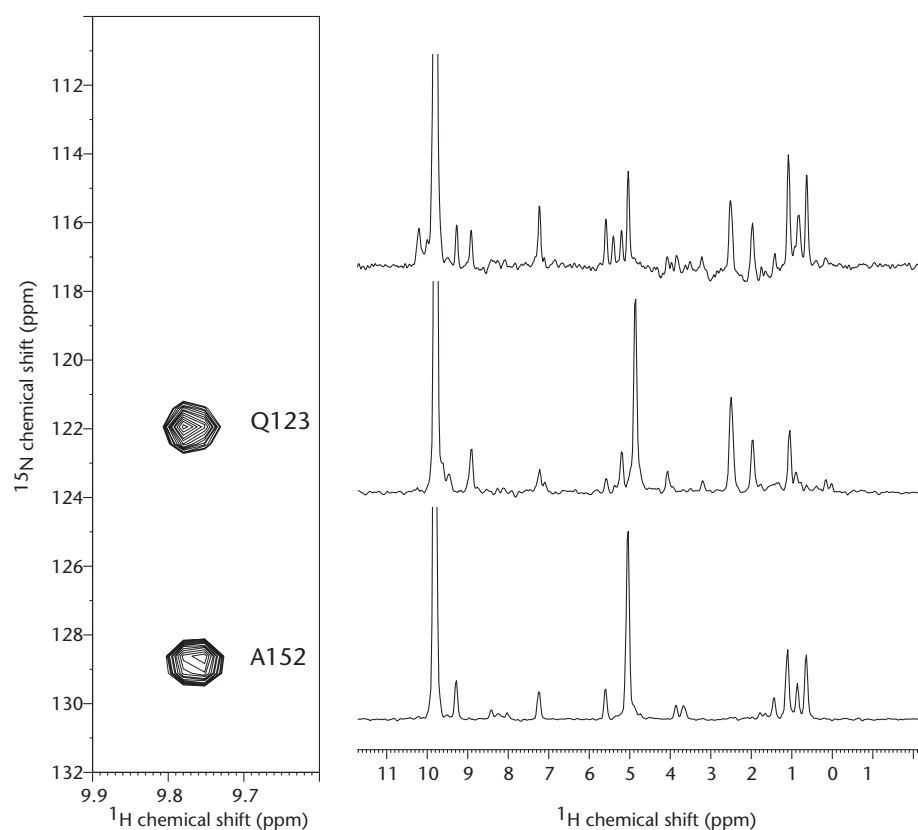
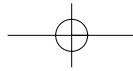


Figure 9.7 Three-dimensional ^{15}N -edited NOESY spectrum of 1 mM ^{15}N -labeled ARD in 90/10 $\text{H}_2\text{O}/\text{D}_2\text{O}$ acquired at 750 MHz. The two-dimensional strip (left) is extracted at 9.75 ppm in the F2 (indirect ^1H) and F3 (observe ^1H) dimensions. The two amide ^{15}N chemical shifts can clearly be seen. On the right are one-dimensional slices through the three-dimensional spectrum at 129 ppm in ^{15}N (bottom), and at 122 ppm in ^{15}N (middle). The top slice is taken from the two-dimensional NOESY shown in Figure 9.3.

There are some general design guidelines that are followed in most three-dimensional NMR experiments currently in use. First, coherence is transferred from ^1H to an X spin at the beginning of the experiment (polarization transfer). After evolution on X (and perhaps further transfer to Y), the coherence is returned to ^1H for detection (**inverse detection**). Since the coherence transfer rate between two spins is proportional to their mutual coupling constant, the most efficient three-dimensional NMR experiments take advantage of coherence transfer between spins coupled with the largest J values. Often, these are one bond couplings. Also, as coherences in large molecules such as proteins or polynucleic acids tend to have short T_2 relaxation times, the time between the first pulse and acquisition is at a premium, and the shortest experiments are usually the most efficient.

As of the time of writing (2006), advances in probe technology and method modifications such as sample deuteration have made these design guidelines somewhat



less general than they were in the 1990s. The use of cryogenically-operated probes (in which the detector coil and preamplifier electronics are helium-cooled to ~35 K in order to reduce thermal noise) provides the potential for direct observation of ^{13}C in multidimensional experiments, so that the back-transfer to ^1H is not always necessary for detection in a three-dimensional experiment. Secondly, many large proteins (>30 kDa in size) are now often prepared with uniform deuteration of non-exchanging ^1H spins, so that transfer from ^{13}C to ^1H is not always possible. Such considerations will be dealt with separately. First, we will summarize some of the most common components of multidimensional multinuclear NMR experiments. Generally, these components can be classified as polarization transfers, evolution (frequency labeling) steps, isotropic mixing, refocusing steps or filters.

Polarization transfer

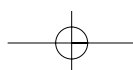
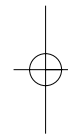
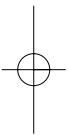
Probably the single most common component of a multidimensional NMR experiment is a polarization transfer from one type of spin to another. This can be accomplished using either an HSQC- or HMQC-type transfer. Generally, HSQC transfers are preferred over HMQC transfers, because of the advantages discussed in Chapter 8. Polarization transfers occur in precisely the fashion described above for the one- and two-dimensional versions of these experiments, with delay times set to optimize polarization transfer for the particular coupling constant of the nuclei involved in the transfer.

The polarization transfer may either be forward (away from proton) or reverse (back to proton). Unless there is more than one proton dimension in the experiment (i.e. an indirectly detected ^1H dimension, usually t_1 , as well as the directly detected ^1H dimension t_3), the first step in a heteronuclear three-dimensional experiment is usually a polarization transfer from ^1H to a heteronucleus. This can involve transfer either to ^{15}N or ^{13}C and provides the sensitivity enhancement inherent in INEPT. In many of the standard experiments for sequential assignment of proteins, the first transfer is from the amide ^1H to the directly bonded ^{15}N . Polarization transfer steps between nuclei other than ^1H are used to correlate two different types of heteronuclei (e.g. ^{15}N and ^{13}C).

Solvent suppression

A typical protein sample for NMR studies contains ~0.5 mM protein and nearly 100 M solvent protons in the form of H_2O ! This presents a serious dynamic range problem, as the digitizer will be filled almost exclusively by the water signal unless something is done to minimize that signal. As such, efficient methods for the suppression of the water signal are essential. Multidimensional NMR experiments can be divided into two groups, homonuclear and heteronuclear experiments, and these generally employ different water suppression techniques.

We will first consider the simpler case of heteronuclear experiments (at least simpler from the point of view of solvent suppression). Such experiments contain polarization transfer steps involving magnetization transfer from ^1H to directly attached heteronuclei (usually ^{15}N or ^{13}C). Since water signals cannot pass through this



transfer filter, the heteronuclear filter provides excellent water suppression, at least when gradient coherence selection is employed (Figure 9.8). It is important to remember that coherence selection by phase cycling requires the acquisition of FIDs in which all of the signals are present, including solvent, and it is only after the FIDs are subtracted by phase cycling that the unwanted signals are removed. This means that dynamic range problems still exist in each FID and must be dealt with, as described below.

Homonuclear experiments must employ some active solvent suppression technique. Originally, **presaturation** (applying a long low power pulse at the water resonance) was the method of choice. The result of this is to equalize the populations of spin states in the solvent, resulting in zero net magnetization for the solvent signal. Although presaturation provides excellent water suppression, the signals of exchangeable protons are also attenuated by presaturation by exchange with the saturated water protons, and this will, through spin diffusion, attenuate even the signals of non-exchangeable protons. While amide NH exchange is suppressed under acidic conditions, many proteins are unstable to acid, so this is not an ideal solution to the problem. Furthermore, protons that resonate near the solvent frequency are

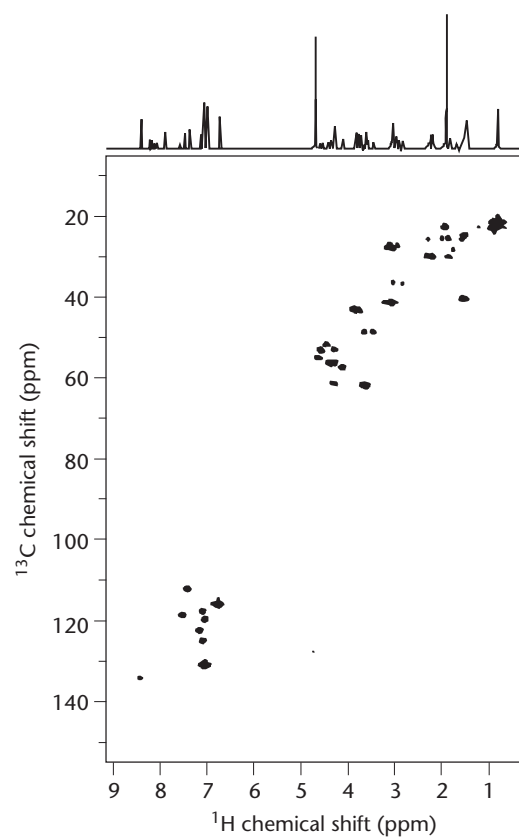


Figure 9.8 Natural abundance ^1H , ^{13}C HMQC spectrum of 5 mM LHRH (leuteinizing hormone-releasing hormone, a 10-residue peptide) in 90/10 $\text{H}_2\text{O}/\text{D}_2\text{O}$. Gradient coherence selection of protons bound to ^{13}C effectively suppresses the water signal (4.8 ppm).

also saturated, including those of non-exchangeable protons of interest in the sample. For proteins, this often includes many of the $C_{\alpha}H$ backbone protons that are critical for sequential assignments. For this reason, presaturation is rarely used in modern pulse sequences. The most widely used alternative to presaturation is WATERGATE (a lovely descriptive name for people of a certain age, since one is trying to “plug” the leak of a water signal!) (Reference 2, Figure 9.9). In WATERGATE, a $\pi/2$ pulse is applied, bringing magnetization into the transverse plane. This pulse is followed by a gradient that dephases all transverse magnetization, including that due to water. An *antiselective* composite π pulse that is designed to have a null at the water frequency is then applied, followed by a second gradient pulse that has the effect of refocusing coherences that have been affected by the π pulse, while the water signal will remain dephased, and will not appear in the detected signal. The WATERGATE element is fairly simple to implement in multidimensional experiments and provides an excellent level of suppression (see Figure 9.10). The details of the WATERGATE sequence will be the focus of a Problem at the end of this chapter.

Another commonly employed improvement in water suppression is the water **flip-back** pulse (Reference 3). Historically, water suppression methods were designed to prevent transverse coherence from developing from the water spins, and there

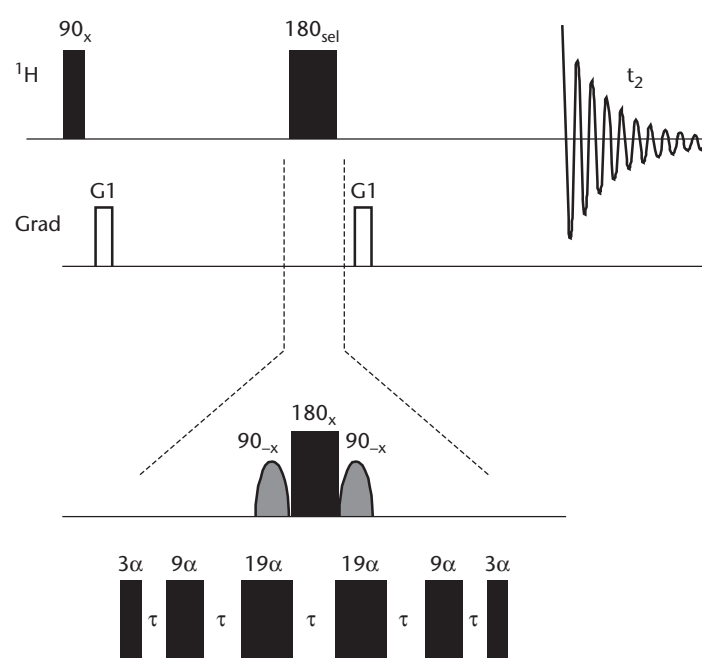


Figure 9.9 Basic WATERGATE element for pulse sequences. Two possible ways of producing the antiselective 180° pulse (exciting all frequencies over a range except that of water) are indicated by the dashed lines. The first employs two soft 90° pulses at the water frequency surrounding a hard 180° pulse. The second employs a binomial-like pulse train (3–9–19) to achieve the null at the water frequency.

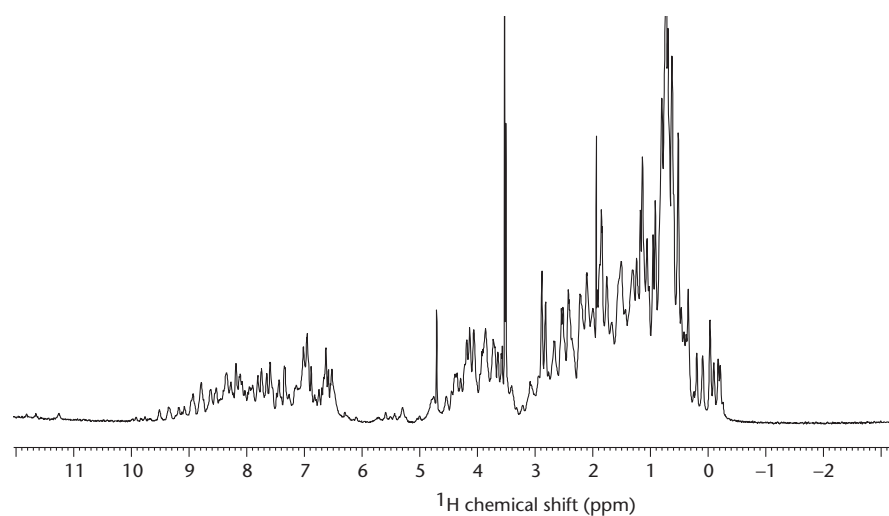
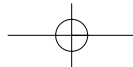
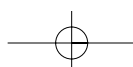


Figure 9.10 600 MHz ^1H spectrum of 1 mM adrenodoxin, a 108-residue ferredoxin, in 90/10 $\text{H}_2\text{O}/\text{D}_2\text{O}$ using WATERGATE for solvent suppression.

was not much interest in where the water magnetization ended up in the course of a pulse sequence as long as it did not produce a signal during acquisition. One problem that can result from improper placement of the water magnetization is **radiation damping**, a phenomenon that is observed when an inherently intense coherence is stored along the $-z$ axis (i.e. as $-\hat{I}_z$). This operator represents a population inversion, and the energy that is stored in this inversion can be released coherently as a result of a self-induced precession in the laboratory frame. This rotates the coherence at the Larmor frequency of the resonance through the x, y plane, until the equilibrium population is restored along $+z$. This coherent emission results in a strong low-frequency ringing in the receiver coil and generates a distorted solvent peak in the spectrum. The process of radiation damping is precisely analogous to what occurs in a laser, in which energy stored as an inverted population over an electronic transition is released as a coherent pulse. A way to avoid radiation damping and other effects that might occur as the result of the state of the water coherence is to apply water-specific soft flip-back pulses to the water signal in order to maintain the water magnetization along the $+z$ axis throughout the pulse sequence. Not only does the flip-back prevent radiation damping, but it also prevents unwanted attenuation of the signals of interest from spin diffusion or chemical exchange with water (as described above for presaturation). An example of an HSQC experiment incorporating water flip-back pulses is shown in Figure 9.11, with a comparison of the results obtained using presaturation and WATERGATE suppression with flip-back pulses shown in Figures 9.12 and 9.13.

Frequency-labeling periods and constant time NMR experiments

The second and third dimensions of three-dimensional experiments require that two indirectly detected time domains, t_1 and t_2 , both independent of the acquisition time (t_3), be built up over the course of the experiment. As each data point in the t_1



252 Multidimensional NMR and biological applications

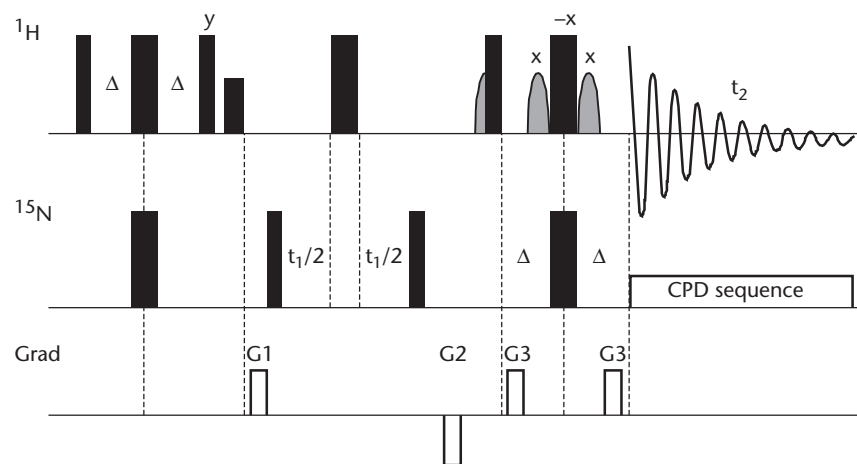


Figure 9.11 Pulse sequence for ^1H , ^{15}N HSQC experiment using WATERGATE for solvent suppression and employing a water flip-back pulse. The water-flip back pulse is indicated by the shaded pulse immediately before the WATERGATE element.

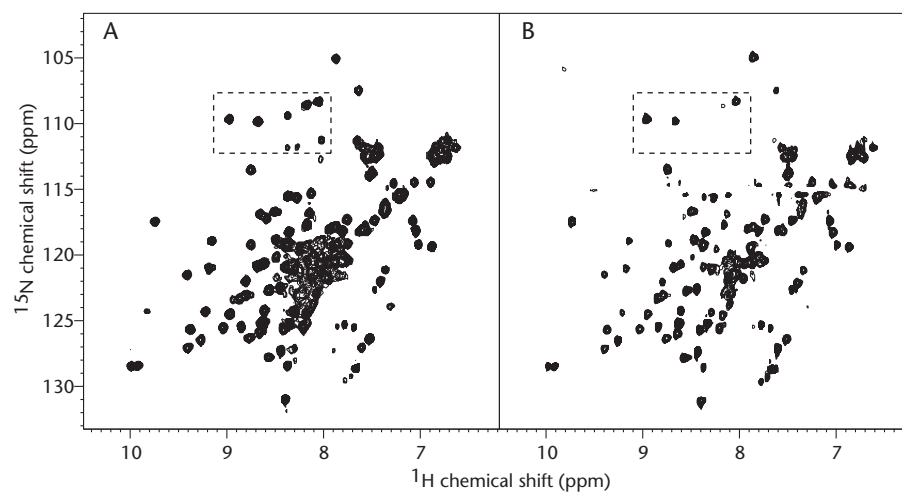


Figure 9.12 ^1H , ^{15}N HSQC spectra of 2 mM putidaredoxin (106 residues, 12.4 kDa molecular weight) in 90/10 $\text{H}_2\text{O}/\text{D}_2\text{O}$. (A) Spectrum was acquired with the pulse sequence shown in Figure 9.11. (B) Spectrum was acquired with presaturation for water suppression. Boxed regions are expanded in Figure 9.13.

and t_2 dimensions requires a separate acquisition, the number of points collected for the indirectly detected dimensions determines the duration of the experiment. In some cases, this can be as long as a week, depending on the sensitivity of the sequence, sample concentration and other variables that control signal-to-noise ratio. Fortunately, large numbers of data points in the indirectly detected dimensions are rarely necessary. While two-dimensional experiments are often acquired with as many as 512 complex points in t_1 , three-dimensional experiments rarely

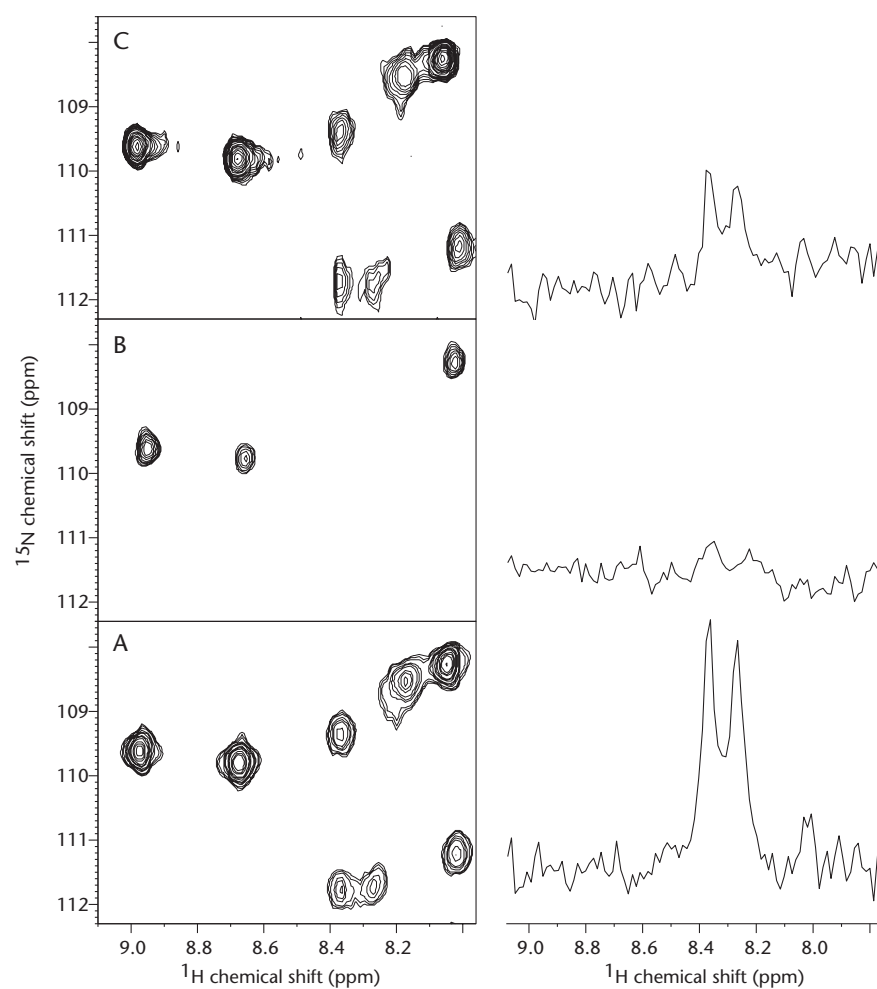
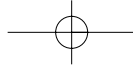


Figure 9.13 Portions of the ^1H , ^{15}N HSQC spectra of 2 mM putidaredoxin in 90/10 $\text{H}_2\text{O}/\text{D}_2\text{O}$ are shown. (A and B) The two-dimensional spectra are the corresponding regions shown with dashed lines in Figure 9.12. (C) The spectrum was acquired with the pulse sequence described in Figure 8.22, employing gradient coherence selection as the only means of water suppression. The one-dimensional slices (^{15}N chemical shift = 111.8 ppm) from each of the two-dimensional spectra clearly demonstrate the improved sensitivity that can be obtained when water is kept along the z axis.

exceed 128 complex points in t_1 or t_2 in order to obtain sufficient resolution for most purposes, and 32 complex points in an indirectly detected dimension are often sufficient.

As with two-dimensional NMR experiments, pure phase and quadrature detection in the indirectly detected dimensions requires either States–Haberkorn or TPPI cycling in these dimensions. Of course, instead of a 2×2 set of data matrices, $2 \times 2 \times 2$ sets are required using the States method (rrr, rri, rir, irr, rii, iri, iir, iii, or the functional equivalent in TPPI). A variation on the States method, commonly called



States-TPPI, modulates the receiver phase by 180° at each increment of the evolution time for a given dimension. This results in axial peaks being shifted from the center of the spectrum to one edge, an advantage of the traditional TPPI method.

The problem with frequency-labeling periods, or evolution periods, is that they get longer as the three-dimensional experiment progresses. This exaggerates relaxation in the latter parts of the experiment, when both t_1 and t_2 (indirectly detected time domain) delays are long. This means that the signal-to-noise ratio of FIDs acquired later in the experiment will suffer from signal loss due to relaxation relative to the earlier FIDs. However, a scheme for minimizing this problem called **constant time evolution** has come into general use (Reference 4). This scheme combines the necessary evil of a relatively long J -coupling evolution for polarization transfer with the chemical shift evolution required for frequency labeling of the spin from which polarization transfer is to occur, thereby saving a step in the experiment. Furthermore, there is no increase in relaxation through the evolution time, so the interferogram that results from the constant time evolution is not affected by relaxation during the constant time evolution, making linear prediction of various types (including “negative time” linear prediction) more useful.

The heart of the constant time evolution scheme is a π pulse on the transverse coherence that “floats” through the J -evolution period during the course of the experiment. In many cases, the constant time evolution period t_1 immediately follows a polarization transfer step from ^1H . Consider the evolution time t_1 that occurs during a J -evolution (polarization transfer) period of duration $2T$. The time before the π pulse has a duration $T + t_1/2$, while the time after the pulse has a duration $T - t_1/2$, so that the first increment occurs with time periods of equal duration before and after the π pulse. The first period increases in duration as t_1 increments, while the second period decreases. It may not be immediately obvious why this results in frequency-labeling of the transverse coherence, so it is helpful to calculate the effect on a single transverse operator, $\hat{\mathbf{I}}_x$. During the first period $T + t_1/2$, $\hat{\mathbf{I}}_x$ evolves as expected with chemical shift (ignoring any coupling evolution):

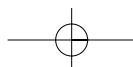
$$\hat{\mathbf{I}}_x \rightarrow \hat{\mathbf{I}}_x \cos \Omega(T + t_1/2) + \hat{\mathbf{I}}_y \sin \Omega(T + t_1/2) \quad (9.1)$$

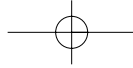
The application of a π_x pulse at this point gives:

$$\hat{\mathbf{I}}_x \rightarrow \hat{\mathbf{I}}_x \cos \Omega(T + t_1/2) - \hat{\mathbf{I}}_y \sin \Omega(T + t_1/2) \quad (9.2)$$

Using the definitions of the Cartesian operators in terms of raising and lowering operators, we can describe the evolution of each term during the second time period (leaving out the modulation during the first period for the moment) with:

$$\begin{aligned} \hat{\mathbf{I}}_x &= \frac{1}{2}(\hat{\mathbf{I}}_+ + \hat{\mathbf{I}}_-) \rightarrow \left(\hat{\mathbf{I}}_+ \exp(-i\Omega(T - t_1/2)) + \hat{\mathbf{I}}_- \exp(i\Omega(T - t_1/2)) \right) \\ \hat{\mathbf{I}}_y &= \frac{1}{2i}(\hat{\mathbf{I}}_+ - \hat{\mathbf{I}}_-) \rightarrow \left(\hat{\mathbf{I}}_+ \exp(-i\Omega(T - t_1/2)) - \hat{\mathbf{I}}_- \exp(i\Omega(T - t_1/2)) \right) \end{aligned} \quad (9.3)$$





Returning to the Cartesian basis:

$$\begin{aligned} & \frac{1}{2} \left(\left[\hat{\mathbf{I}}_x + i\hat{\mathbf{I}}_y \right] \exp(-i\Omega(T - t_1/2)) + \left[\hat{\mathbf{I}}_x - i\hat{\mathbf{I}}_y \right] \exp(i\Omega(T - t_1/2)) \right) \\ & - \frac{1}{2i} \left(\left[\hat{\mathbf{I}}_x + i\hat{\mathbf{I}}_y \right] \exp(-i\Omega(T - t_1/2)) - \left[\hat{\mathbf{I}}_x - i\hat{\mathbf{I}}_y \right] \exp(i\Omega(T - t_1/2)) \right) \end{aligned} \quad (9.4)$$

Collecting terms, and using the relationships between trigonometric and complex exponentials to convert to trigonometric functions:

$$\begin{aligned} & \hat{\mathbf{I}}_x \cos(\Omega(T - t_1/2)) + \hat{\mathbf{I}}_y \sin(\Omega(T - t_1/2)) \\ & + \hat{\mathbf{I}}_x \cos(\Omega(T - t_1/2)) - \hat{\mathbf{I}}_y \sin(\Omega(T - t_1/2)) \end{aligned} \quad (9.5)$$

These two equations represent the evolution expected after the π pulse. Multiplying by the modulation terms that evolved prior to the π pulse, we obtain:

$$\begin{aligned} & \left\{ \hat{\mathbf{I}}_x \cos(\Omega(T - t_1/2)) + \hat{\mathbf{I}}_y \sin(\Omega(T - t_1/2)) \right\} (\cos(\Omega(T + t_1/2))) \\ & + \left\{ \hat{\mathbf{I}}_x \sin(\Omega(T - t_1/2)) - \hat{\mathbf{I}}_y \cos(\Omega(T - t_1/2)) \right\} (\sin(\Omega(T + t_1/2))) \end{aligned} \quad (9.6)$$

Using the trigonometric relationships that relate multiplication of sines and cosines, the following terms are obtained:

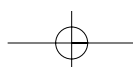
$$\begin{aligned} & \hat{\mathbf{I}}_x \left[\frac{1}{2} \cos(\Omega(T + t_1/2 - T + t_1/2)) + \frac{1}{2} \cos(\Omega(T + t_1/2 + T - t_1/2)) \right] \\ & + \hat{\mathbf{I}}_x \left[\frac{1}{2} \cos(\Omega(T + t_1/2 - T + t_1/2)) - \frac{1}{2} \cos(\Omega(T + t_1/2 + T - t_1/2)) \right] \\ & \hat{\mathbf{I}}_y \left[\frac{1}{2} \sin(\Omega(T + t_1/2 - T + t_1/2)) + \frac{1}{2} \sin(\Omega(T + t_1/2 + T - t_1/2)) \right] \\ & - \hat{\mathbf{I}}_y \left[\frac{1}{2} \sin(\Omega(T - t_1/2 - T - t_1/2)) - \frac{1}{2} \sin(\Omega(T - t_1/2 + T + t_1/2)) \right] \end{aligned} \quad (9.7)$$

The last terms in each of the four lines in the preceding equation cancel, leaving only the sums of the first terms, that yield:

$$\hat{\mathbf{I}}_x \cos(\Omega t_1) + \hat{\mathbf{I}}_y \sin(\Omega t_1) \quad (9.8)$$

i.e. the evolution expected of a normally incremented t_1 period.

The choice of the length of the constant time evolution delay is critical. Usually, the constant time evolution involves product operators of the type $\hat{\mathbf{I}}_x \hat{\mathbf{S}}_z$ that are generated by polarization transfer to spin \mathbf{I} from spin \mathbf{S} at the beginning of the evolution period. The length of the constant time evolution ($2T$) is chosen so as to preserve a particular characteristic of the coherence as it was in the beginning of the constant time evolution. For example, in the CT-HNCA experiment shown in Figures 9.14 and 9.15, $2T$ is set to $1/J_{NH}$, so that the antiphase character of the $\hat{\mathbf{N}}_x \hat{\mathbf{H}}_z$ coherence



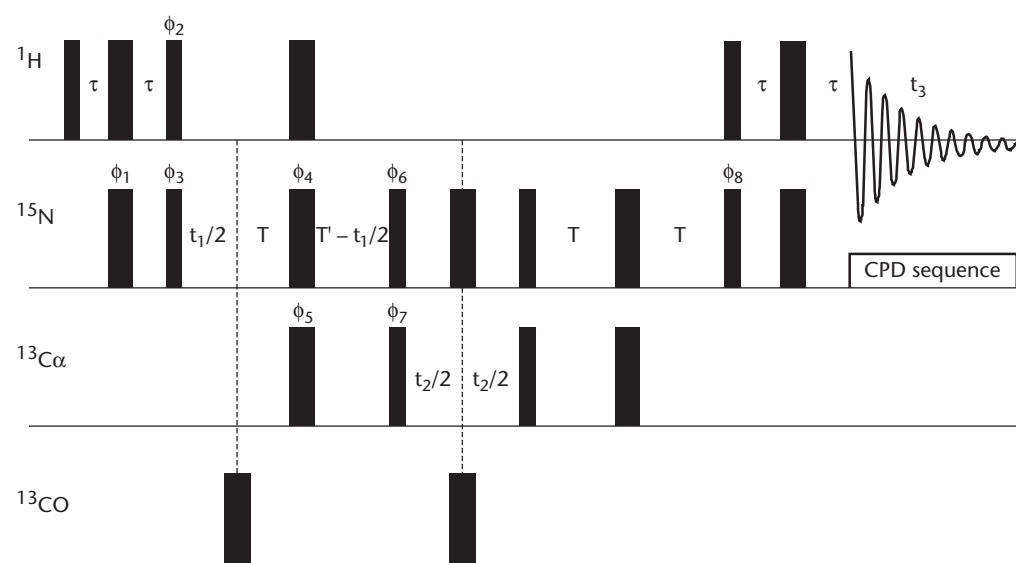


Figure 9.14 Diagram of a constant time phase-cycled HNCA experiment. Narrow lines represent $\pi/2$ pulses, broad lines represent π pulses. Delays are set as follows: $\tau = 1/4J_{NH}$, $2T = 1/J_{NH}$, $T' = T + \text{length of the } \pi \text{ pulse on } C = O$. Phase cycling is: $\phi 1: x, -x$; $\phi 2: y, -y$; $\phi 3: x$; $\phi 4: r(x), 4(y), 4(-x), 4(-y)$; $\phi 5: 16(x), 16(-x)$; $\phi 6: 16(y), 16(-y)$; $\phi 7: x, -x, -x, x$; $\phi 8: y$; Acq: $=2(x, -x, -x, x, -x, x, x, -x), 2(-x, x, x, -x, x, -x, -x, x)$.

that is generated after the first polarization transfer (from ^1H to ^{15}N) is maintained during the subsequent periods and is refocused only at the end of the sequence, in time for detection during t_3 .

A limitation of the constant time method is that, as the frequency-labeling period is limited by the polarization transfer step, digital resolution in the corresponding dimension is limited by the length of the coupling evolution time $2T$. The length of the t_1 increment (the dwell time) is determined by the spectral width, so only a fixed number of points can be acquired during $2T$, determined by $2T/(\text{dwell})$.

Shaped and selective pulses

Since the chemical-shift range covered by various types of ^{13}C nuclei (e.g. aliphatic, carbonyl, etc.) is wide and the shift differences between these various types can be large, most heteronuclear experiments treat carbonyl, aromatic and sp^3 -hybridized ^{13}C separately. ^{13}C pulses are usually designed to be sufficiently selective so that only one type of carbon spin is excited per pulse. For this reason, one often sees polarization transfer steps between different types of carbon atoms in multidimensional NMR experiments. The simplest way to achieve this selectivity is to apply a rectangular pulse centered on the frequency of interest, with the pulse length and power adjusted to produce an excitation null at the other carbon frequencies of interest. For example, in an experiment that correlates carbonyl carbons with C_α carbons, an ideal pulse would affect a $\pi/2$ rotation for the ^{13}CO spins while resulting in a 2π

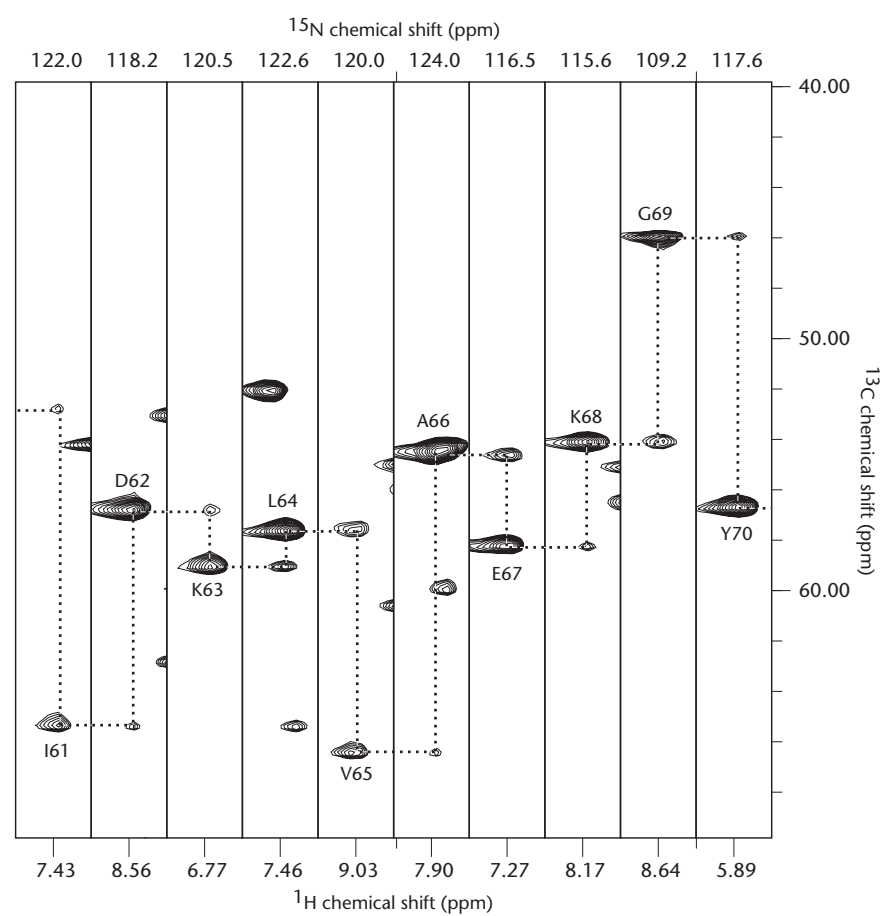


Figure 9.15 Strips from the constant time HNCA spectrum of 1 mM ^{15}N , ^{13}C -labeled ARD (acireductone dioxygenase) in 90% $\text{H}_2\text{O}/\text{D}_2\text{O}$ acquired at 500 MHz. A sequential walk from isoleucine 61 through tyrosine 70 is shown.

(null) rotation for the $^{13}\text{C}_\alpha$ spins. Using the frame of reference shown in the figure in Problem 3.11 and performing the calculations as in Chapter 3 (Problem 10.3) we obtain the following results:

$$PW_{90} = \frac{\sqrt{15}}{4\Delta B} \quad \text{and} \quad PW_{180} = \frac{\sqrt{3}}{2\Delta B} \quad (9.9)$$

where ΔB is the chemical-shift separation in Hz between ^{13}CO and $^{13}\text{C}_\alpha$. The expression for PW_{180} describes the requirement for a π pulse on ^{13}CO with a null at $^{13}\text{C}_\alpha$.

Implicit in the above discussion is the assumption that one can switch the center frequency of a pulse rapidly in the course of a pulse sequence, so that if we wish to excite carbonyl carbons with the carrier frequency set at $^{13}\text{C}_\alpha$, we could employ a frequency jump immediately prior to center the excitation on the ^{13}CO region.

Theoretically, this is possible; however, on the majority of spectrometers, this would result in a loss of phase coherence, thereby leading to spectral artifacts (see Figure 9.16). A cleaner approach is to apply a phase ramp to the selective pulse to achieve an effective frequency change. Practically, the selective pulse is created digitally in the electronics by dividing it into small increments (i.e. points) that can be phase- and amplitude-modulated individually. If we desire to excite carbonyls while our transmitter remains at the frequency of $^{13}\text{C}_\alpha$, we use the following equation to calculate the phase advance of each of the pulse units:

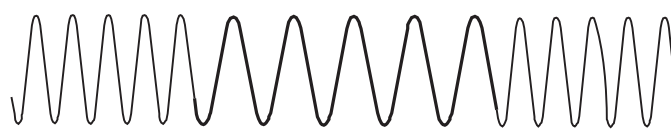
$$\left(\frac{\theta}{360}\right)\left(\frac{1}{\tau}\right) \equiv \Delta\omega \quad (9.10)$$

where $\Delta\omega$ is the difference between the transmitter and the desired frequency, τ is the length of the selective pulse divided by the number of points used to create the pulse digitally, and θ is the phase increment necessary to achieve the frequency shift (Figure 9.17). Construction of such a pulse is the subject of Problems 9.3 and 9.4.



Figure 9.17 A selective pulse can be divided into small elements (points), with the minimum length of each element determined by the spectrometer hardware. The sum of the elements (τ) is the total length of the pulse. To achieve off-resonance excitation, each element will have a phase increment (θ) determined as in Equation 9.10.

Synchronous frequency shift



Asynchronous frequency shift

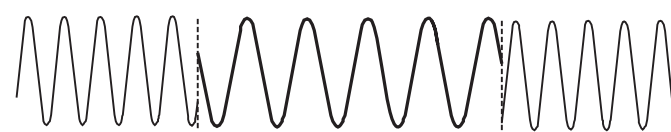


Figure 9.16 Synchronous versus asynchronous frequency-shifting. Pulses generated at different frequencies (or different power levels, as in decoupling) can either be synchronous with each other (that is, continuous phase advance) or asynchronous (discontinuous with respect to phase).

From the basic elements described above, virtually all of the published triple-resonance experiments have been built. An analysis of these elements found in a standard triple resonance experiment HN(CO)CA is shown in Figure 9.18.

Composite pulse decoupling and spin-locking

One final but very important consideration in multidimensional NMR experiment design is the use of *composite pulse decoupling* (CPD). This topic was introduced in Chapter 7, but it is worth talking about it here too, since the efficiency of decoupling can determine the success of a given experiment and indeed the safety of the NMR sample and probe. It is often necessary to decouple one type of spin from another for reasons of reducing spectral complexity and improving the signal-to-

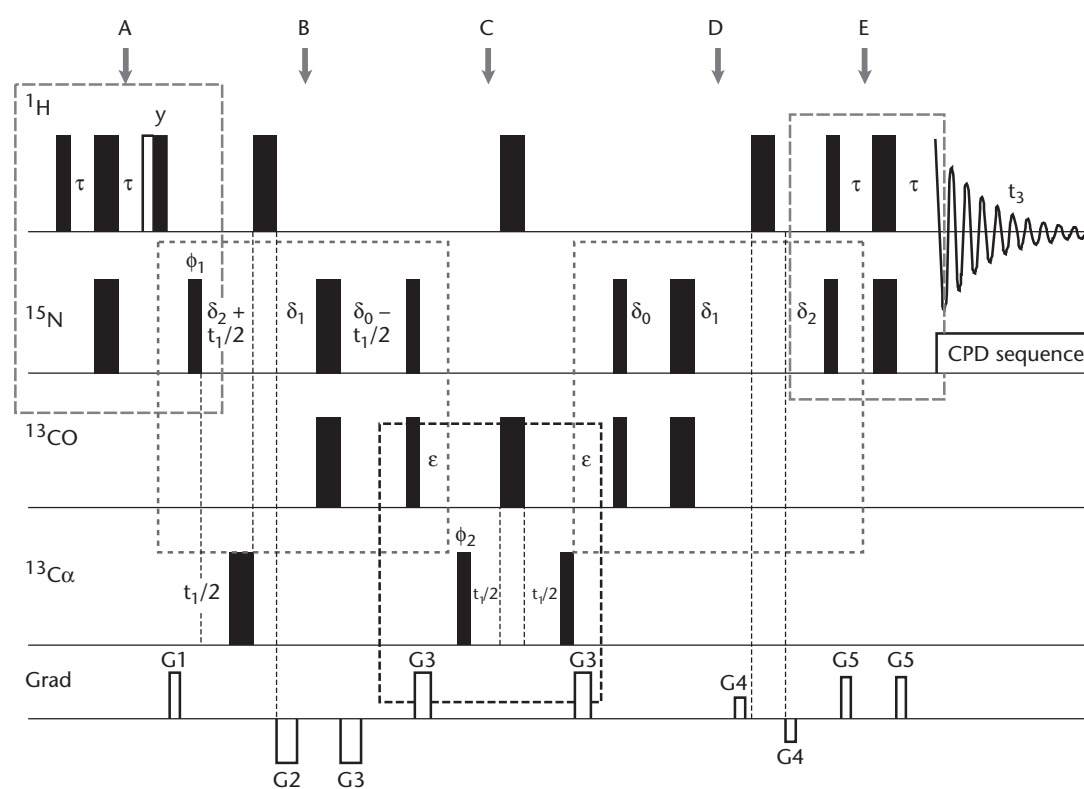


Figure 9.18 HN(CO)CA pulse sequence illustrating the incorporation of basic elements such as polarization transfer into multidimensional experiments. (A) INEPT transfer from amide protons to amide nitrogen, with crusher gradient. (B) Constant time evolution for ^{15}N coherence, with coherence transfer to carbonyl carbon, while refocusing coupling due to ^1H and C_α . (C) HMQC transfer from carbonyl carbon to C_α , followed by frequency labeling at C_α shift, and return to carbonyl carbon. (D) Reverse transfer from carbonyl carbon to ^{15}N , followed by (E) reverse INEPT to ^1H for detection. Pulse sequence details are as follows: $\tau = 2.25$ ms [$2\tau = 1/(2J_{\text{NH}})$], $\delta_0 = 12$ ms [$2\delta_0 = 1/(3J_{\text{NCO}})$], $\delta_1 = 9.25$ ms, $\delta_2 = 2.75$ ms [$2\delta_2 = 1/(2J_{\text{NH}})$], $\varepsilon = 6.6$ ms [$\varepsilon = 1/(3J_{\text{C}_\alpha\text{CO}})$], $G_1 = G_5 = 150$ μs at 9 G/cm, $G_2 = 1.5$ ms at 9 G/cm, $G_3 = 450$ μs at 9 G/cm, $G_4 = 100$ μs at 3.5 G/cm. G_1 is a “crusher” gradient that dephases any coherence in the transverse plane while the desired coherences are stored along the z axis. Quadrature detection is achieved by incrementing ϕ_1 and ϕ_2 (in t_1 and t_2 , respectively).

noise ratio. In almost every heteronuclear two- and three-dimensional experiment, heteronuclei are decoupled from ^1H during acquisition using broadband CPD sequences, so that only ^1H singlets are observed. However, even prior to acquisition, CPD is often applied for a variety of reasons, including spin-locking. In the HCCH-TOCSY experiment, for example, coherence is generated first on ^1H and then transferred via a polarization transfer step to a directly bonded ^{13}C . At this point, a CPD sequence is applied that spin-locks the appropriate ^{13}C spins with the frequency-labeling information from the original ^1H passed to other ^{13}C atoms in the spin

system via Hartmann–Hahn transfer. (Because direct ^{13}C – ^{13}C couplings are used for magnetization transfer rather than two- and three-bond couplings, spin-lock times are considerably shorter in ^{13}C Hartmann–Hahn transfers than for ^1H transfers over the same spin systems.) After the spin-locking CPD is turned off, the ^{13}C spins are released to evolve with free precession during t_2 , and then coherence is transferred back to the attached ^1H spins via a back polarization transfer for detection during t_3 . The resulting three-dimensional spectrum correlates ^1H spins with multiple carbons in the same spin system (e.g. all part of the same amino acid side chain in a protein), providing a powerful tool for making identification of side chain spin systems (Figure 9.19).

A wide variety of CPD sequences are available, and some are more suited to particular tasks than others. The schemes can be sorted by whether they are **synchronous** (i.e. phase-coherent with pulses that precede and follow the CPD sequence) or **asynchronous**. For spin-locking, as in TOCSY and HCCH-TOCSY, it is necessary to insure that CPD is synchronous, because the states of the spins before and

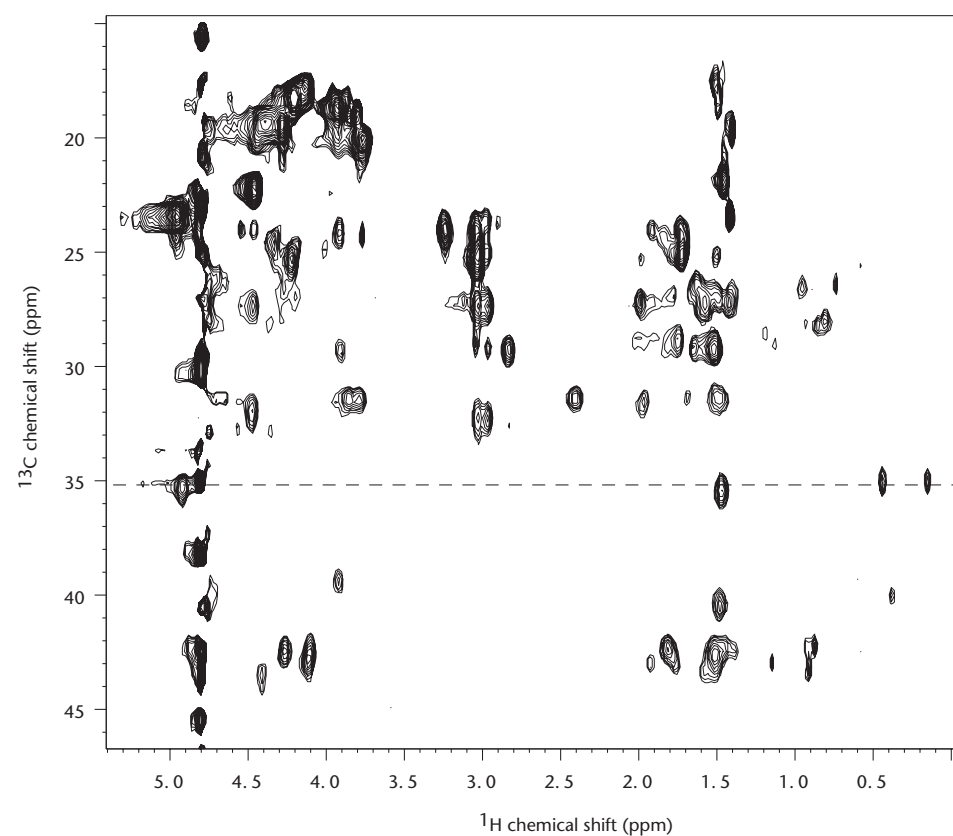


Figure 9.19 ^1H , ^{13}C -Plane taken at 1.44 ppm (indirect proton dimension) from the three-dimensional HCCH-TOCSY spectrum of 1 mM ^{15}N , ^{13}C -labeled ARD (acireductone dioxygenase) in 90% $\text{H}_2\text{O}/\text{D}_2\text{O}$ acquired at 600 MHz. The dashed line indicates the V122 spin system. The ^{13}C shift of 35.3 ppm corresponds to the C_β resonance ($^1\text{H}_\beta$ is at 1.44 ppm). Correlations can be seen from the C_β to the H_γ and H_α .

after the CPD sequence are critical for the success of the experiment. That is, the spins that are detected are those that have been subjected to the spin lock. However, when all one wants to do is remove the effects of coupling, synchronous CPD can result in artifacts, sometimes called “decoupling sidebands”, that result from the generation of unwanted coherences. In this case, the use of asynchronous decoupling (random phase shifts relative to what occurs before or after the CPD) insures that any artifacts resulting from the decoupling are not reinforced during signal averaging.

All CPD sequences incorporate “inversion elements” (pulse trains that result in population inversions of the decoupled spins) that are repeated or combined so as to return spins to their starting configurations, so that the time-averaged magnetization of the decoupled spins is zero. The sequences are typically designed to provide uniform excitation profiles over a desired chemical-shift range. The particular sequence employed depends on the spin to be decoupled and the frequency range over which the decoupling is to be deployed. For ^1H decoupling and spin locking, some long-standing sequences that are still widely used are MLEV and WALTZ decoupling schemes (References 5 and 6). Because the ^1H chemical shift range is fairly narrow, the correct bandwidth profile is relatively easy to achieve, and the major concern for ^1H decoupling is to insure that only as much power is applied as is required for a particular task. Too much power can result in sample heating, particularly for samples that are at high ionic strength.

For other nuclei, particularly ^{13}C , decoupling is a much more demanding business. Because ^{13}C chemical-shift ranges are large and increase with field, simple rectangular pulse decoupling (i.e. the pulses composing the CPD are of a length so as to excite a particular bandwidth) can be problematic at higher fields, requiring shorter pulses at high powers in order to obtain the needed excitation profile. Off-resonance effects (tip angles near the edge of the excitation envelope different from that at the center) also become more serious. With the introduction of ^{13}C spin-locking experiments such as HCCH-TOCSY, it was found that if composite pulses were used to compensate for off-resonance effects, excitation profiles were more even over the effective range of the decoupling. One commonly employed CPD sequence that incorporates composite pulses is DIPSI (Reference 7), that has been employed with great success for both ^1H and ^{13}C spin-locking.

As magnetic fields get larger, it becomes more difficult to use hard pulse trains for CPD. The increased bandwidth requires shorter pulses at higher power to obtain the same spectral excitation envelope, so arcing of probes (i.e. sparking across the coils during a pulse) becomes a significant problem. In answer to this, a new generation of CPD sequences based on **adiabatic** pulses has entered into use. Unlike hard pulses that are formed from a single frequency and whose excitation envelope depends upon pulse length, adiabatic pulses incorporate a frequency sweep along with amplitude modulation to insure that spins of different chemical shifts are excited to the same degree. Adiabatic pulses can be used to perform relatively uniform excitation for a given group of spins despite variations in chemical shift. Such pulses are named for the adiabatic condition, in which the rate of tip of the spin due to the pulse is slow compared to the spin's precessional frequency. This “slow passage”

allows the precession of spins to track the B_1 field accurately due to the applied RF, with less sensitivity to chemical-shift effects.

The most popular CPD sequences incorporating adiabatic pulses are the plumply named WURST series (Reference 8). The WURST sequences provide fairly wide and uniform excitation bandwidths with lower power requirements than for hard pulse sequences with similar excitation envelopes. These have become the CPD sequences of choice for applications requiring broadband decoupling such as HCCH-TOCSY at high magnetic fields.

Dealing with very large biomolecules in solution: deuteration and direct ^{13}C detection

In addition to all of the other problems that are encountered in biological NMR (i.e. large solvent signals, chemical exchange, low sample concentrations and signal overlap), the very nature of the observed NMR signals from biological macromolecules hampers the experiment. In Chapter 4, the importance of the correlation time in determining the relaxation behavior of nuclear spins was discussed. As molecules increase in size, they tumble more slowly and the spin-spin interactions that result in T_2 relaxation become more efficient. In turn, this leads to line-broadening and decrease in the effective lifetimes of coherences that are generated at the beginning of a multiple-pulse NMR sequence. A more complete discussion of the theory and interpretation of relaxation phenomena as applied to biological molecules will be found in Chapter 11. However, for now it is enough to point out that for protein molecules more than ~30 kDa effective molecular weight, ^1H T_2 relaxation rates are short enough to seriously degrade the efficiency of coherence transfer for most multidimensional NMR experiments.

A number of approaches have been used to circumvent the apparent 30 kDa limit on NMR characterization of proteins. The most straightforward, at least in principle, is the use of random deuteration to dilute the number of ^1H spins present in the molecule. ^1H spins are the primary source of dipole-dipole relaxation for other protons as well as ^{13}C and ^{15}N spins. If a sample of protein is prepared using perdeuterated growth medium (usually by overexpression in bacterial or other cultured cells), most of the nonexchangeable protons (i.e. those bonded to carbon) will be replaced by ^2H . ^2H has a much lower gyromagnetic ratio than ^1H , and is not as efficient at promoting dipole-dipole relaxation in nearby nuclei. This results in a significant line-narrowing for the remaining ^1H spins (typically the amide NH groups that exchange with buffer during purification/refolding in protonated medium). While ^2H does exhibit observable couplings with other spins (and those couplings show up as triplets, since the $\mathbf{I} = 1$ ^2H nucleus has three accessible spin states) one-bond coupling constants of ^2H are much smaller than the corresponding one-bond couplings to ^1H . Furthermore, the chemical-shift range of ^2H is considerably smaller than that even of ^1H , so decoupling of ^2H during evolution and detection periods is usually a simple matter.

The most obvious drawback to perdeuteration is that the same spins that are usually used for polarization transfer in standard triple-resonance NMR experiments (i.e. those

correlating ^1H , ^{15}N and ^{13}C) as well as those used for NOEs in structure determination are no longer there. As such, some important and useful NMR experiments that require a high density of ^{13}C -attached ^1H spins (e.g. HCCH-TOCSY and ^1H , ^{13}C HSQC-NOESY) are not useful for such samples. Furthermore, for proteins that are not amenable to refolding, even nominally exchangeable protons attached to ^{15}N that are not solvent accessible will not be detected. In recent years, a large number of sequences that are specifically designed for use with deuterated proteins have been developed.

Another important development has been the introduction of probes in which transceiver coils and preamplifiers are cryogenically cooled by helium gas ("cold probes" or "cryoprobes", depending on the manufacturer). This cooling (to $\sim 35\text{ K}$) results in the reduction of thermal noise in critical detector/preamplifier circuitry, and in the case of ^1H detection, this can give up to 4-fold improvement in S/N, so lower concentrations of sample can be used. This is important for experiments with biological macromolecules of low intrinsic solubility (e.g. membrane proteins) or of high molecular weight. The use of cryogenically cooled probes equipped with a cooled ^{13}C preamplifier has permitted the introduction of a new class of two-dimensional and three-dimensional NMR experiments that employ direct detection of ^{13}C . Typically used with uniformly ^{13}C and ^{15}N labeled and deuterated or partially deuterated macromolecules, such experiments bypass the time-consuming polarization steps from and to ^1H required by ^1H -detected experiments, yielding a series of relatively simple two-dimensional and three-dimensional pulse sequences that correlate ^{13}C and ^{15}N directly (References 9 and 10). These experiments take advantage of the relatively long relaxation times of deuterated ^{13}C spins, permitting multiple-spin correlations even in large ($>40\text{ kDa}$) proteins.

Interference patterns in heteronuclear relaxation: TROSY

In Chapter 4, we discussed the primary mechanisms for relaxation of $\mathbf{I} = 1/2$ nuclei in solution and the dependence of these mechanisms upon the correlation time, τ_c . The correlation time provides a measure of the rate at which the molecule reorients in the magnetic field, and can be thought of as the mean time required for a molecule to reorient 1 rad in any direction. Recall that nuclear spin relaxation is induced by the time-dependent fluctuations in the local electromagnetic environment, and that slow tumbling encourages low frequency transitions, while faster tumbling can also encourage higher frequency transitions. [One can make the analogy with pulses: short pulses, corresponding to rapid motions of a molecule, have broad excitation bandwidths, and long pulses (slower motions) have fewer frequency components.] Spin-spin interactions that result in line-broadening (T_2) in large molecules such as proteins are typically dominated by the low-frequency terms [zero-quantum transitions $k_0 \propto r_{IS}^{-6} J(\omega_I - \omega_S)$ as shown in Equation 4.11]. These transitions result in the incoherent transfer of magnetization between spins and consequently a loss of macroscopic signal at the time of acquisition.

Another important source of relaxation, particularly at higher magnetic fields such as those commonly used for NMR of macromolecules, is chemical-shift anisotropy (CSA). Recall that CSA is the result of incomplete averaging of the chemical-shift tensor to a scalar quantity (the observed chemical shift) as a function of molecular

tumbling. As the molecule reorients and the chemical shift of a spin is perturbed, time-dependent fluctuations of the spacing of the energy levels of that spin take place, resulting in relaxation. Again, the rate at which the molecule tumbles, as well as the spacing of the energy levels (a function of the strength of the magnetic field employed) modulate the efficiency of CSA relaxation. CSA relaxation is particularly effective for nuclei that are not in a symmetric electronic environment (more p-orbital than s-orbital character of the bonding electrons) such as ^{13}C and ^{15}N . These nuclear spins typically show large differences in chemical shift for different types of environments, and as field strengths increase, CSA may become a dominant relaxation mechanism for such spins.

The fluctuating fields due to CSA and dipole–dipole (dd) interactions at a given spin have directionality as well as frequency. As a molecule tumbles, the CSA and dd fields superimpose at the position of the spin under consideration and can interfere with each other in a constructive or destructive fashion, a phenomenon known as **cross-correlation**. For example, if two spin $1/2$ nuclei, I and S , are dipole-coupled to each other, spin I can detect spin S in two possible states, $|\alpha\rangle$ and $|\beta\rangle$. The sign of the dipolar field at I is determined by the spin state of S , and as such, the cross-correlation terms between the CSA and dd terms will have opposite signs depending upon which transition of spin I is being observed, that in which the coupled S spin is $|\alpha\rangle$ and that in which spin S is $|\beta\rangle$. For one I transition (corresponding to one of the two lines in the I doublet resulting from scalar coupling to S), the cross-correlation term will enhance relaxation, but for the other I transition, it will make relaxation less efficient. The net result of this is different line widths for the two lines of the IS doublet, reflecting the differential relaxation of the two transitions of I . An example of such differential broadening is shown in Figure 9.20, and a readable

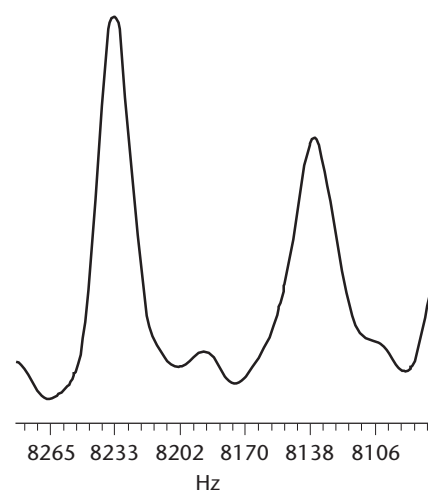


Figure 9.20 A slice taken through the ^1H dimension of the ^1H , ^{15}N HSQC spectrum of 1 mM ^{15}N -labeled ARD in 90% $\text{H}_2\text{O}/\text{D}_2\text{O}$ acquired at 600 MHz showing a ^1HN signal split by J_{NH} (~ 95 Hz). The HSQC was acquired without decoupling during t_1 , so the ^{15}N coupling is clearly visible. The line widths are considerably different.

description of this phenomenon as applied to a ^{15}N - ^1H pair can be found in Reference 11.

The differential broadening becomes particularly interesting when one considers the implications for a two-dimensional heteronuclear experiment such as HSQC. Under normal circumstances, refocusing of the coupling during t_1 evolution on I by placing a π pulse on S at $t_1/2$ as well as decoupling of I during acquisition (t_2) results in singlet structure in both dimensions for the observed correlation between I and S in the transformed two-dimensional spectrum. As a result, any differential line broadening is lost. However, if one performs the HSQC experiment without refocusing or decoupling in either dimension, one would obtain, for a simple coupled IS pair, a set of four peaks, split by $^1J_{IS}$ in both dimensions. As in the one-dimensional experiment shown in Figure 9.21, the peaks would show the effects of differential line-broadening in both dimensions. For one of the four peaks, the cross-terms in both dimensions would reinforce the CSA and dd relaxation, resulting in very efficient relaxation (with a correspondingly broad line). For two of the peaks, the cross-terms would be opposite in sign during t_1 and t_2 , resulting in an intermediate line width after transformation. For the fourth peak, the cross-terms would both interfere destructively with the other relaxation terms, resulting in a narrower line width in both dimensions. If one could select for just this line in the quartet, the size of molecules amenable to multidimensional NMR methods using HSQC-type correlations for detection could be considerably increased. Such selection is the basis of the TROSY (transverse relaxation optimized spectroscopy) experiment first described by Pervushin *et al.* (Reference 12). The TROSY pulse sequence (Figure 9.21) is designed to select only the transition in which the cross-correlation terms suppress T_2 relaxation in both time domains. Figures 9.22 and 9.23 show the implementation of TROSY.

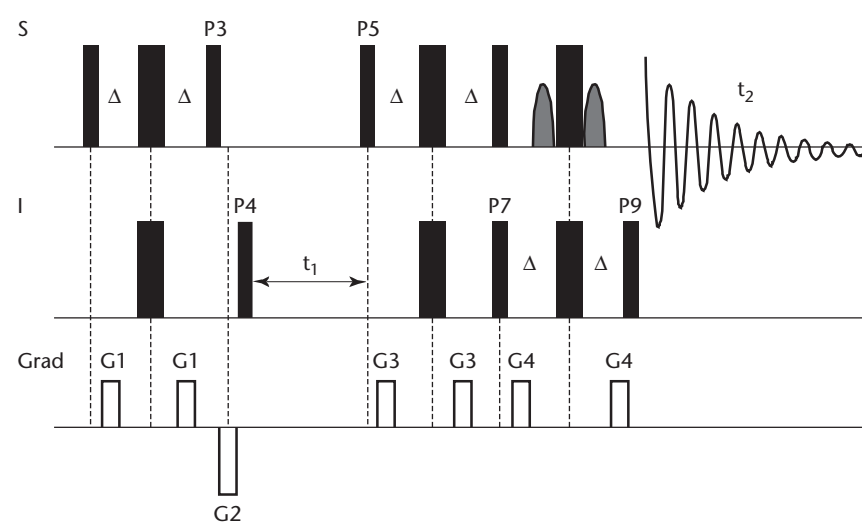


Figure 9.21 Pulse sequence of the TROSY experiment. $\Delta = 1/4J_{NH}$ phases on all pulses are x except as follows (eight-step phase cycle). P3: $8\{y\}$. P4: $\{y, -y, -x, x, y, -y, -x, x\}$. P5: $4\{y\}, 4\{-y\}$. P7: $8\{y\}$. P9: $4\{x\}, 4\{-x\}$. Receiver: $\{x, -x, -y, y, x, -y, y\}$. Gradients with the same label have the same intensity and duration. The gradient between P3 and P4 is a “crusher gradient”.

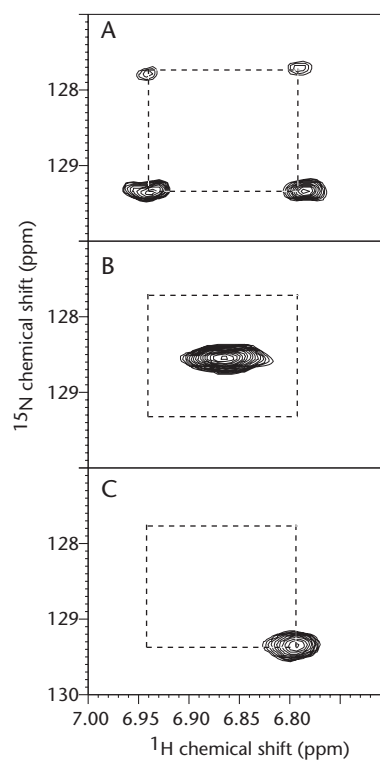


Figure 9.22 (A) ^1H , ^{15}N HSQC correlation from oxidized cytochrome P450_{cam}, a 414-residue monomeric heme-containing enzyme, acquired without refocusing of the $^1J_{\text{NH}}$ coupling in ω_1 and without decoupling of ^{15}N in ω_2 , showing the different line widths of individual components of the multiplet due to interference of dd and CSA relaxation (see text). (B) Same correlation, but with refocusing of the $^1J_{\text{NH}}$ -coupling in ω_1 and decoupling of ^{15}N in ω_2 . (C) Same correlation but with TROSY phase cycling to remove all but the narrowest line of the multiplet.

In order to analyze the TROSY sequence, we need to expand the density matrix in terms of a new basis set that is convenient for describing single transitions (corresponding to single lines in the NMR experiment). Recall that the Cartesian basis is convenient for describing the evolution of coherences under the influences of pulses and \mathbf{z} -directed operators, while the single-element basis allows one to determine the evolution of particular orders of coherence under a variety of influences. However, in TROSY, we are concerned with differential effects upon single transitions that would otherwise behave identically under the influences of pulses and \mathbf{z} -directed operators. For this purpose, we need to observe the evolution of the density matrix using the **single-transition basis** set.

Consider the two $I = 1/2$ spins of the IS spin system with transitions as diagrammed in Figure 9.24. We wish to consider individual transitions within this diagram, for

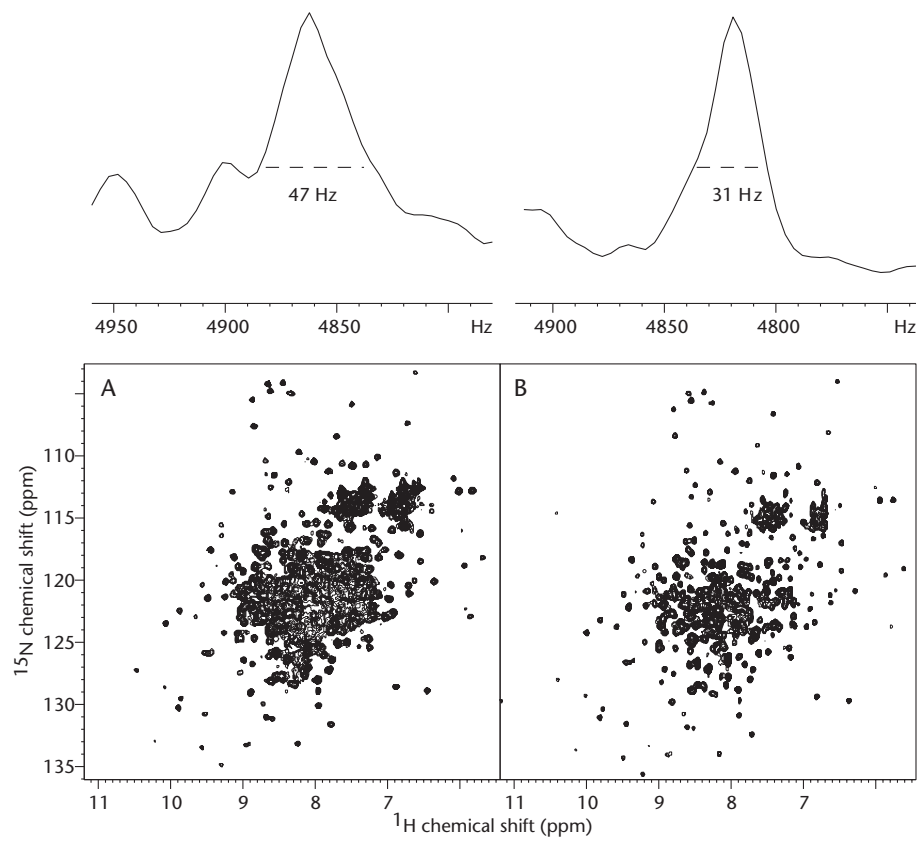


Figure 9.23 (A) ^1H , ^{15}N HSQC spectrum of oxidized cytochrome P450_{cam} obtained at 600 MHz ^1H with the line width of a single correlation in ω_2 shown above the spectrum. (B) TROSY version of the same spectrum, showing the reduced line width for the same correlation as in (A).

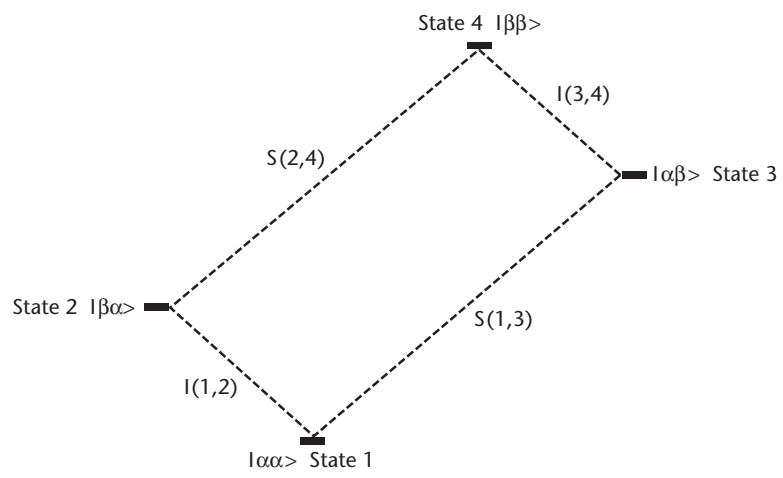
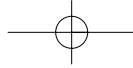


Figure 9.24 Diagram of transitions in the single-transition basis for the IS doublet.



example $\mathbf{I}(1,3)$ or $\mathbf{S}(1,2)$. The single-transition operators are defined relative to the Cartesian and single-element operator basis sets as:

$$\begin{aligned}
 \hat{\mathbf{S}}_x^{(1,2)} &= \hat{\mathbf{I}}_\alpha \hat{\mathbf{S}}_x & \hat{\mathbf{S}}_y^{(1,2)} &= \hat{\mathbf{I}}_\alpha \hat{\mathbf{S}}_y & \hat{\mathbf{S}}_+^{(1,2)} &= \hat{\mathbf{I}}_\alpha \hat{\mathbf{S}}_+ & \hat{\mathbf{S}}_-^{(1,2)} &= \hat{\mathbf{I}}_\alpha \hat{\mathbf{S}}_- \\
 \hat{\mathbf{S}}_x^{(3,4)} &= \hat{\mathbf{I}}_\beta \hat{\mathbf{S}}_x & \hat{\mathbf{S}}_y^{(3,4)} &= \hat{\mathbf{I}}_\beta \hat{\mathbf{S}}_y & \hat{\mathbf{S}}_+^{(3,4)} &= \hat{\mathbf{I}}_\beta \hat{\mathbf{S}}_+ & \hat{\mathbf{S}}_-^{(3,4)} &= \hat{\mathbf{I}}_\beta \hat{\mathbf{S}}_- \\
 \hat{\mathbf{I}}_x^{(1,3)} &= \hat{\mathbf{I}}_x \hat{\mathbf{S}}_\alpha & \hat{\mathbf{I}}_y^{(1,3)} &= \hat{\mathbf{I}}_y \hat{\mathbf{S}}_\alpha & \hat{\mathbf{S}}_-^{(1,2)} &= \hat{\mathbf{I}}_\alpha \hat{\mathbf{S}}_- & \hat{\mathbf{I}}_-^{(1,3)} &= \hat{\mathbf{I}}_- \hat{\mathbf{S}}_\alpha \\
 \hat{\mathbf{I}}_x^{(2,4)} &= \hat{\mathbf{I}}_x \hat{\mathbf{S}}_\beta & \hat{\mathbf{I}}_y^{(2,4)} &= \hat{\mathbf{I}}_y \hat{\mathbf{S}}_\beta & \hat{\mathbf{S}}_-^{(3,4)} &= \hat{\mathbf{I}}_\beta \hat{\mathbf{S}}_- & \hat{\mathbf{I}}_-^{(2,4)} &= \hat{\mathbf{I}}_- \hat{\mathbf{S}}_\beta
 \end{aligned} \tag{9.11}$$

The superscripted (i, j) indicate the particular transitions that each operator represents, as shown in Figure 9.24. Note that all of these product operators are the result of the combination of a population operator on one spin and a raising or lowering operator on the other. We will also need the relationships between polarization operators and the identity operator given in Equation 6.15:

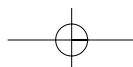
$$\begin{aligned}
 \hat{\mathbf{I}}_z &= \frac{1}{2}(\hat{\mathbf{I}}_\alpha - \hat{\mathbf{I}}_\beta) \\
 \frac{1}{2}\hat{\mathbf{I}} &= \frac{1}{2}(\hat{\mathbf{I}}_\alpha + \hat{\mathbf{I}}_\beta) \\
 \hat{\mathbf{I}}_\alpha &= \frac{1}{2}\hat{\mathbf{I}} + \hat{\mathbf{I}}_z \\
 \hat{\mathbf{I}}_\beta &= \frac{1}{2}\hat{\mathbf{I}} - \hat{\mathbf{I}}_z
 \end{aligned} \tag{9.12}$$

With these definitions in hand, we can consider how the TROSY experiment results in cancellation of the broader components of the IS multiplet, while reinforcing the narrow component. At first, the experiment proceeds as the normal HSQC experiment. The initial $\pi/2$ pulse on ^1H (S) gives $-\hat{\mathbf{S}}_y$ that evolves through the first polarization transfer (up through P4) to $2\hat{\mathbf{I}}_x \hat{\mathbf{S}}_z$. Expanding this in terms of raising and lowering operators, one obtains $\hat{\mathbf{I}}_+ \hat{\mathbf{S}}_z + \hat{\mathbf{I}}_- \hat{\mathbf{S}}_z$. Using the relationships shown in Equations 9.11, this can in turn be expanded into the single-transition basis as:

$$\begin{aligned}
 \hat{\mathbf{I}}_\pm^{(1,2)} &= \frac{1}{2}\hat{\mathbf{I}}_\pm + \hat{\mathbf{S}}_z \hat{\mathbf{I}}_\pm \\
 \hat{\mathbf{I}}_\pm^{(3,4)} &= \frac{1}{2}\hat{\mathbf{I}}_\pm - \hat{\mathbf{S}}_z \hat{\mathbf{I}}_\pm
 \end{aligned} \tag{9.13}$$

The time evolution of the single-element operators on the right-hand sides of Equation 9.13 during t_1 results in the following set of terms (ignoring relaxation):

$$\begin{aligned}
 &\frac{1}{2}\hat{\mathbf{I}}_- (\exp[i\omega_{12}t_1] - \exp[i\omega_{34}t_1]) \\
 &+ \hat{\mathbf{S}}_z \hat{\mathbf{I}}_- (\exp[i\omega_{12}t_1] + \exp[i\omega_{34}t_1]) \\
 &\frac{1}{2}\hat{\mathbf{I}}_+ (\exp[-i\omega_{12}t_1] - \exp[-i\omega_{34}t_1]) \\
 &+ \hat{\mathbf{S}}_z \hat{\mathbf{I}}_+ (\exp[-i\omega_{12}t_1] + \exp[-i\omega_{34}t_1])
 \end{aligned} \tag{9.14}$$



The subsequent polarization transfer back to spin S , prior to evolution during acquisition (t_2) results in the following observable terms:

$$\begin{aligned} & \frac{1}{2} \hat{\mathbf{S}}_- \left(i \cos[\omega_{12} t_1] - \sin[\omega_{12} t_1] \right) \\ & - \hat{\mathbf{S}}_- \hat{\mathbf{I}}_z \left(i \cos[\omega_{12} t_1] - \sin[\omega_{12} t_1] \right) \\ & + \frac{1}{2} \hat{\mathbf{S}}_- \left(i \cos[\omega_{34} t_1] + \sin[\omega_{34} t_1] \right) \\ & + \hat{\mathbf{S}}_- \hat{\mathbf{I}}_z \left(i \cos[\omega_{34} t_1] + \sin[\omega_{34} t_1] \right) \end{aligned} \quad (9.15)$$

Not explicitly shown in Expressions 9.14 and 9.15 are the associated relaxation exponentials, that differ between the terms associated with transition ω_{12} and ω_{34} . Notice that the two terms associated with ω_{12} have opposite signs, while those associated with ω_{34} have the same sign. This difference can be exploited via phase cycling to select only for ω_{12} -associated terms, so that after the eight steps of the phase cycle shown in Figure 9.21, only the following terms remain (now with the relaxation exponentials shown explicitly):

$$\begin{aligned} & -4 \hat{\mathbf{S}}_- \sin[\omega_{12} t_1] \exp[-R_{12} t_1] \\ & + 8 \hat{\mathbf{S}}_- \hat{\mathbf{I}}_z \sin[\omega_{12} t_1] \exp[-R_{12} t_1] \end{aligned} \quad (9.16)$$

This will correspond to the hyper-real portion of the interferogram that will eventually yield the ω_1 dimension of the TROSY experiment. A $\pi/2$ phase shift of P4 at each value of t_1 gives the hyper-imaginary portion, as usual with States quadrature detection experiments. The two operators in Equation 9.16 will evolve during t_2 to give the following expressions:

$$\begin{aligned} \hat{\mathbf{S}}_- & \rightarrow \left(\exp[i\omega_{13} t_2 - R_{13} t_2] + \exp[i\omega_{24} t_2 - R_{24} t_2] \right) \\ 2 \hat{\mathbf{S}}_- \hat{\mathbf{I}}_z & \rightarrow \left(\exp[i\omega_{13} t_2 - R_{13} t_2] - \exp[i\omega_{24} t_2 - R_{24} t_2] \right) \end{aligned} \quad (9.17)$$

Combining expressions 9.16 and 9.17 gives the density operator element for the single desired component of the IS multiplet:

$$\sigma_{12,24} \rightarrow 8 \left(\exp[i\omega_{12} t_1 + i\omega_{24} t_2] + \exp[-(R_{12} t_1 + R_{24} t_2)] \right) \quad (9.18)$$

The TROSY sequence can be incorporated into virtually any three-dimensional experiment in which an HSQC-type transfer is used for polarization transfer prior to detection, yielding a suite of experiments with TROSY modifications that can be used for high-resolution NMR work with very large proteins. At present, high-resolution structure determination using these methods is still problematic; nevertheless the availability of sequential assignments provides a way of examining details of large protein structure and dynamics in solution.

Problems

- 9.1** Show that $2\hat{I}_x\hat{S}_z$ can be expanded into Equation 9.15 using the definitions of the single element operators. Show the evolution of the single element terms during t_1 of TROSY, and then recombine the terms back into the Cartesian basis.
- *9.2** Triple resonance experiments based on the ^1H , ^{15}N HSQC pulse sequence often incorporate “crusher gradients” to remove unwanted transverse magnetization while maintaining the desired coherence transfer pathways. Such gradients are usually very short, and placed between the two 90 degree pulses used to convert $2\hat{S}_x\hat{I}_z$ to $2\hat{S}_z\hat{I}_x$ prior to t_1 evolution on ^{15}N . Why is this? Use operators to explain your answer.
- *9.3** Using Equations 9.9 and 9.10, design an off-resonance pulse square pulse consisting of 32 steps, that will invert ^{13}C carbonyl resonances (~ 180 ppm) without affecting C_α carbons (~ 60 ppm) at 600 MHz ^1H frequencies. What is the phase increment at each step?
- 9.4** If one wanted to make the pulse in Problem 9.3 a 90° pulse (tip angle of $\pi/2$) rather than an inversion pulse at the carbonyl carbon, but still a null at the C_α resonance, how long should the total pulse be? What is the phase increment for each step?
- 9.5** A problem that one often runs into while setting up two-dimensional and three-dimensional experiments is setting the proper phase corrections in the indirectly detected dimensions for processing. Not only can this mean a tedious processing and reprocessing until each dimension is correctly phased, but first-order phase corrections can result in a significant baseline distortion (called “baseline roll”). The origins of the phenomenon lie in the fact that RF pulses have a finite width, and signals of different chemical shifts will change their phase under the influence of the pulse at different rates, resulting in a frequency-dependent phase advance by the time the end of the first sampling period [$t_1(0)$] is reached. In the old days, this problem was dealt with by scaling the first FID [corresponding to $t_1(0)$] prior to transformation in t_1 , often by multiplication by 0.5, or by back-predicting that point using linear prediction. However, some simple considerations in setting up the experiment can minimize this problem without post-acquisition processing [Bax *et al.*, *J. Magn. Reson.* 91, 174–178 (1991)]. If the acquisition delay τ is known, the appropriate first-order phase correction ϕ_1 in the ω_1 dimension can be calculated by $\phi_1 = \tau/\Delta t_1 \times 360^\circ$. So for an acquisition delay τ that is 1/2 the dwell time Δt_1 , a linear phase correction of 180° will give pure-phase spectra in ω_1 without any need to scale the first point. The value of τ can be calculated for a simple 90° pulse of duration t_{90} as $\tau = 4t_{90}/\pi + \Delta t_1(0)$, where $\Delta t_1(0)$ is a programmable delay time for the first t_1 increment. Rearrangement gives this expression $\Delta t_1(0) = 1/(2SW) - 4t_{90}/\pi$ for the desired phase correction. For a NOESY experiment with a t_{90} of 7.3 μs and a 10 kHz spectral width (SW), what should the $\Delta t_1(0)$ be set to in order to have a preset first-order phase correction of 180° ? How about for an HMQC experiment with a ^{15}N sweep width of 2000 Hz and a ^{15}N t_{90} of 35 μs ? Don't forget to include the ^1H 180° pulse width (you can use 14.6 μs) in the calculation, since the t_1 period is divided by the ^1H 180° pulse.

- 9.6** Setting correct RF pulse lengths and powers is critical for maximum sensitivity in three-dimensional experiments. Since direct observation of ^{15}N and ^{13}C (X) is often inconvenient for dilute biological samples, 90° pulses for such nuclei are often set by using the simple sequence: $\pi/2_y(^1\text{H})-\tau(1/2J_{XH})$ -pulse (X)-observe (^1H). The $\pi/2$ X pulse is determined by systematically changing the length (at fixed power) or power (at a fixed length) of the X pulse and watching for a null in the signal of ^1H coupled to X. Using product operators, describe what one is observing in this experiment.
- *9.7** Most modern NMR spectrometers are equipped with linear RF amplifiers, for which simple linear calibrations allow one to predict the $\pi/2$ pulse length as a function of amplifier output. Amplifier output is usually described in decibels (dB), which is a logarithmic measure of the ratio of the total available power to the output power (measured in watts, or joule/s), i.e. $\text{dB} = 10 (\log P_2/P_1)$. Based on this scale, halving output power results in a +3 dB change in attenuation. It is a commonly used rule of thumb that a +6 dB change in attenuation doubles the length of the $\pi/2$ pulse. Based on this, what is the change in $\pi/2$ pulse length one might expect as one goes from 50 W to 35 W pulse power if the pulse length at 50 W is 7 μs ?
- 9.8** Analyze the HN(CO)CA sequence shown in Figure 9.18 in terms of product operator evolution at the end of each component of the sequence as indicated by the dotted lines.
- *9.9** Analyze the WATERGATE pulse train involving two soft water pulses flanking the central hard π pulse shown in Figure 9.9. In particular, consider what is happening to water magnetization in the presence of the field gradients applied during the sequence.
- *9.10** The HN(CO)CA experiment is relatively more sensitive at 600 MHz (^1H) than it is at 800 MHz (^1H), all parameters being otherwise equivalent. The HNCA experiment does not undergo as large a drop in relative sensitivity upon changing fields. Speculate on a reason for this.

References

1. D. Marion, L. E. Kay, S. W. Sparks, D. A. Torchia, and A. Bax, *J. Am. Chem. Soc.* 111, 1515 (1989).
2. M. Piotto, V. Saudek, and V. Sklenár, *J. Biomol. NMR* 2, 661 (1992).
3. S. Grzesiek and A. Bax, *J. Am. Chem. Soc.* 115, 12593 (1993).
4. G. W. Vuister and A. Bax, *J. Magn. Reson.* 98, 428 (1992).
5. R. Freeman, T. Frenkiel, and M. H. Levitt, *J. Magn. Reson.* 50, 345 (1982).
6. A. J. Shaka, J. Keeler, T. Frenkiel, and R. Freeman, *J. Magn. Reson.* 52, 335 (1983).
7. A. J. Shaka, C. J. Lee, and A. Pines, *J. Magn. Reson.* 77, 274 (1988).
8. E. Kupce and R. Freeman, *J. Magn. Reson. Ser. A* 115, 273 (1995).
9. A. Fletschy, O. Moreira, H. Kovacs, and K. Pervushin, *J. Biomol. NMR* 26, 167 (2003).
10. W. Bermel, I. Bertini, I. C. Felli, M. Piccioli, and R. Pierattelli, *Prog. NMR Spectr.* 48, 25 (2006).
11. M. Guéron, J. L. Leroy, and R. H. Griffey, *J. Am. Chem. Soc.* 105, 7262 (1983).
12. K. Pervushin, R. Riek, G. Wider, and K. Wuthrich, *Proc. Natl. Acad. Sci. USA* 94, 12366 (1997).

